# An Improved Direct Power Control for Doubly Fed Induction Generator

Gao, Shuning; Zhao, Haoran; Gui, Yonghao; Zhou, Dao; Blaabjerg, Frede

*Published in:*
I E E E Transactions on Power Electronics

*DOI (link to publication from Publisher):*
10.1109/TPEL.2020.3024620

*Publication date:*
2021

*Document Version*
Accepted author manuscript, peer reviewed version

# An Improved Direct Power Control for Doubly Fed Induction Generator

Shuning Gao, *Student Member, IEEE*, Haoran Zhao, *Senior Member, IEEE*, Yonghao Gui, *Senior Member, IEEE*, Dao Zhou, *Senior Member, IEEE* and Frede Blaabjerg, *Fellow, IEEE*

***Abstract*—A novel Voltage Modulated Direct Power Control (VM-DPC) is firstly designed for a Back-to-Back (BTB) converter in the Doubly Fed Induction Generator (DFIG) system. The proposed VM-DPC is built in the stator stationary reference frame ($\alpha\beta$). The proposed method uses a simple feed-forward and feedback structure without a phase-locked loop and the Park transformation. Therefore, it can be easily implemented in the BTB converter. Another essential advantage of the proposed VM-DPC is that it can transform the closed-loop DFIG system into a linear-time-invariant one, which can be analyzed and designed through multiple linear control techniques. The proposed method guarantees exponential stability in the stiff grid as well as in weak-grid integration, which is proved based on eigenvalue analysis. Simulation results demonstrate that the proposed VM-DPC has a faster transient response than conventional Vector Oriented Control (VOC). Also, it maintains a satisfactory steady-state performance at the same level as the VOC. The robustness of proposed VM-DPC against distorted voltage conditions and parameter mismatch is also tested. Finally, the proposed VM-DPC control strategy is validated in an experimental hardware prototype of a 7.5 kW DFIG system operating in real-time.**

***Index Terms*—Doubly fed induction generator (DFIG), direct power control (DPC), transient response, steady-state.**

## I. Introduction

DUE to the increasing consideration of the fossil energy crisis nowadays, a renewable energy source such as wind power has received worldwide attention. Among the existing wind turbines, the Doubly Fed Induction Generator (DFIG) is one of the mainstream topologies, accounting for around 50% of the total wind-energy market [1]. It has superiorities such as flexible power control capability, low cost of the Back-to-back (BTB) converter, and high reliability [2]–[4]. The increasing wind power penetration level also raises the demand for the control performance of the DFIG. According to the modern grid requirements, the DFIG should not only obtain fast and robust power regulation capability but also, operate under different grid conditions [5], [6].

This work was supported by the National Key R&D Program of China (2018YFB0904004) *(Corresponding author: Haoran Zhao).*

S. Gao is with the School of Electrical Engineering, Shandong University, Jinan 250061, China, and was also with the Automation & Control Section at the Department of Electronic Systems, Aalborg University, 9220 Aalborg, Denmark (email:gaosn@mail.sdu.edu.cn).

H. Zhao is with the School of Electrical Engineering, Shandong University, Ji'nan 250061, China (email:hzhao@sdu.edu.cn).

Y. Gui is with Automation & Control Section at the Department of Electronic Systems, Aalborg University, 9220 Aalborg, Denmark (e-mail:yg@es.aau.dk).

D. Zhou and F. Blaabjerg are with Department of Energy Technology, Aalborg University, 9220 Aalborg, Denmark (e-mail:zda@et.aau.dk, fbl@et.aau.dk).

Generally, the control strategies of the DFIG are designed based on Vector Oriented Control (VOC) or Direct Power Control (DPC). The VOC requires a decoupling of three-phase components in a synchronous rotational reference frame by using a Phase-locked loop (PLL) [7]–[9]. The control structure is based on Linear Time-Invariant (LTI) characteristics, which can be analyzed by using the linear control method structure [10]. However, the performance and stability of the DFIG controlled by VOC are highly dependent on the performance of the PLL and the tuning of the control parameters.

Direct Power Control (DPC) technique can provide DFIG with direct power regulation capability. It avoids PLL and complex parameters tuning in the traditional VOC, which has been widely discussed in recent years [11]–[21]. The conventional DPC utilizes a Look-Up Table (LUT) structure to select switching signals [11]. The switching frequency of LUT based DPC is not fixed but changes over time, which usually results in power and electrical torque pulsations [22]. Model Predictive Control (MPC)-DPC is an improved DPC strategy that has recently been applied in DFIG [23], [24]. The control effect of MPC-DPC is guaranteed by a optimal selection of the voltage vector. However, the evaluation of the optimal control vector is time-consuming, which adds additional computational burden to the control system.

Several studies suggest combining the DPC methods with conventional modulation techniques to guarantee a constant switching frequency. The Sliding Mode Control (SMC)-DPC is a robust control method [25], which has been implemented in DFIG [15], [26]. It obtains a fast power convergence speed and a high robust property against DFIG parameters mismatch. However, it usually brings a power chattering problem [21], [27]. A Back-Stepping (BS) algorithm combined with direct power control is developed in [18], which has a simple structure and obtains satisfactory steady-state performance. However, a zero steady-state error of BS-DPC can hardly be obtained when there is disturbances or model mismatch since it only uses proportional control. A coordinated (C)-DPC without PLL is proposed in [17]. The method replaces the PLL by using a virtual phase signal for coordinate transformation. It features excellent steady-state performance, which was initially sensitive to a grid frequency deviation. The Voltage Modulated (VM)-DPC is a recently proposed simple yet effective control technique for voltage source converters [27]. It guarantees fast and reliable active and reactive power regulation. Moreover, it makes the controlled system Linear-Time-Invariant (LTI), which has been employed in various applications [28]–[34]. However, the implementation of VM-

DPC in DFIG has not been thoroughly discussed.

Motivated by [34], in this paper, the GVM-DPC is employed to the Grid Side Converter (GSC). Then, a novel VM-DPC is designed for the Rotor Side Converter (RSC). Consequently, the main contribution of the paper is that a robust yet straightforward method (VM-DPC) is designed for the BTB converter in the DFIG system, which has the following key features:

1) LTI system with DPC. The proposed VM-DPC transforms the DFIG system into an LTI one, which can be analysed and designed through various linear control techniques.
2) Simple and easy implementation. The proposed control algorithm uses a simple feed-forward and feed-back structure design. Moreover, since the PLL and the Park transformation for both GSC and RSC are unnecessary, it can be expected that the structure and computation can be simplified compared with the VOC.
3) Guaranteed exponential stability. It is proved that the proposed VM-DPC can stabilize the DFIG under the weak-grid integration scenario by using eigenvalue analysis, which is not easy to obtain by using other DPC methods.
4) Improved performance. The proposed VM-DPC has a faster transient response than conventional VOC. Also, it maintains a satisfactory steady-state performance at the same level as the VOC. In addition, the robustness of the proposed method against parameter mismatch and distorted grid condition is verified.

The rest of the paper is organized as follows: in Section II, the detailed mathematical models of the RSC and GSC in the $\alpha\beta$ reference frame are presented. Section III describes the controller design. Section IV provides a stability analysis of DFIG with the proposed VM-DPC. Section V presents the simulation results, which show comparisons among the proposed VM-DPC, the conventional VOC, the C-DPC and the SMC-DPC strategies. Experimental test is presented in Section VI. Finally, the conclusions are given in Section VII.

## II. Overview of DFIG Mathematical Modelling

The mathematical models of RSC and GSC implemented in the $\alpha\beta$ reference frames are analyzed in this section to understand how the proposed VM-DPC directly control the stator active and reactive power by modifying the rotor voltage space vector.

By referring the space vectors in the $\alpha\beta$ reference frame, the stator side and rotor side voltage are represented as follows,

$$\begin{cases} \boldsymbol{v}_{\mathrm{s}}^{\mathrm{s}} = R_{\mathrm{s}}\boldsymbol{i}_{\mathrm{s}}^{\mathrm{s}} + \dfrac{\mathrm{d}\boldsymbol{\psi}_{\mathrm{s}}^{\mathrm{s}}}{\mathrm{d}t} \\ \boldsymbol{v}_{\mathrm{r}}^{\mathrm{s}} = R_{\mathrm{r}}\boldsymbol{i}_{\mathrm{r}}^{\mathrm{s}} + \dfrac{\mathrm{d}\boldsymbol{\psi}_{\mathrm{r}}^{\mathrm{s}}}{\mathrm{d}t} - j\omega_{\mathrm{e}}\boldsymbol{\psi}_{\mathrm{r}}^{\mathrm{s}} \end{cases} \tag{1}$$

where $\omega_{\mathrm{e}}$ is the electrical angular frequency of rotor, $R_{\mathrm{s}}$ and $R_{\mathrm{r}}$ represent stator and rotor resistances, superscript 's' of vectors indicates the $\alpha\beta$ reference frame, which is omitted in the rest of this paper for simplicity, $\boldsymbol{v}_{\mathrm{s}}$ and $\boldsymbol{v}_{\mathrm{r}}$ represent the stator and rotor voltage space vector, $\boldsymbol{i}_{\mathrm{s}}$ and $\boldsymbol{i}_{\mathrm{r}}$ represent stator and rotor current space vectors. $\boldsymbol{\psi}_{\mathrm{s}}$ and $\boldsymbol{\psi}_{\mathrm{r}}$ represent the stator and rotor flux space vectors, respectively. The flux linkage and current relation in the stator and the rotor side are expressed as,

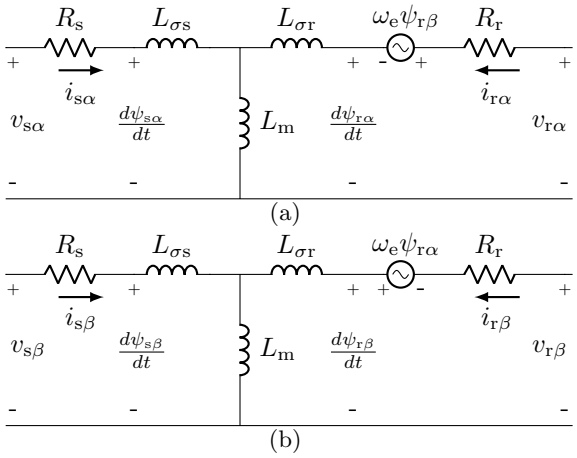


Fig. 1. Equivalent circuit diagram of DFIG. (a) Equivalent circuit in the $\alpha$ reference frame. (b) Equivalent circuit in the $\beta$ reference frame.

$$\begin{cases} \boldsymbol{\psi}_{\mathrm{s}} = L_{\mathrm{s}}\boldsymbol{i}_{\mathrm{s}} + L_{\mathrm{m}}\boldsymbol{i}_{\mathrm{r}} \\ \boldsymbol{\psi}_{\mathrm{r}} = L_{\mathrm{r}}\boldsymbol{i}_{\mathrm{r}} + L_{\mathrm{m}}\boldsymbol{i}_{\mathrm{s}} \end{cases} \tag{2}$$

where $L_{\mathrm{s}}$ and $L_{\mathrm{r}}$ are total self-inductance of the stator and rotor windings, respectively, $L_{\mathrm{m}}$ is the mutual inductance. The equivalent electrical diagram of DFIG in the $\alpha\beta$ reference frame can be concluded, as shown in Fig. 1. By manipulating (2), $\boldsymbol{i}_{\mathrm{r}}$ is eliminated and the rotor flux linkage is expressed as follows,

$$\boldsymbol{\psi}_{\mathrm{r}} = \sigma L_{\mathrm{m}}\boldsymbol{i}_{\mathrm{s}} + \frac{L_{\mathrm{r}}}{L_{\mathrm{m}}}\boldsymbol{\psi}_{\mathrm{s}} \tag{3}$$

where $\sigma = 1 - \frac{L_{\mathrm{s}}L_{\mathrm{r}}}{L_{\mathrm{m}}^2}$ is defined as the leakage factor. By manipulating (1), (2) and (3), the relationship between stator/rotor currents, stator/rotor voltages and stator flux can be deduced as follows,

$$\begin{aligned} \boldsymbol{v}_{\mathrm{r}} - \frac{L_{\mathrm{r}}}{L_{\mathrm{m}}}\boldsymbol{v}_{\mathrm{s}} =& R_{\mathrm{r}}\boldsymbol{i}_{\mathrm{r}} + \sigma L_{\mathrm{m}}\frac{\mathrm{d}\boldsymbol{i}_{\mathrm{s}}}{\mathrm{d}t} - j\omega_{\mathrm{e}}(\sigma L_{\mathrm{m}}\boldsymbol{i}_{\mathrm{s}} \\ &+ \frac{L_{\mathrm{r}}}{L_{\mathrm{m}}}\boldsymbol{\psi}_{\mathrm{s}}) - \frac{R_{\mathrm{s}}L_{\mathrm{r}}}{L_{\mathrm{m}}}\boldsymbol{i}_{\mathrm{s}} \end{aligned} \tag{4}$$

The space vector mentioned above are expressed by the components in the $\alpha\beta$ reference frame as: $\boldsymbol{v}_{\mathrm{s}} = v_{\mathrm{s}\alpha} + jv_{\mathrm{s}\beta}$, $\boldsymbol{v}_{\mathrm{r}} = v_{\mathrm{r}\alpha} + jv_{\mathrm{r}\beta}$, $\boldsymbol{i}_{\mathrm{s}} = i_{\mathrm{s}\alpha} + ji_{\mathrm{s}\beta}$, $\boldsymbol{i}_{\mathrm{r}} = i_{\mathrm{r}\alpha} + ji_{\mathrm{r}\beta}$, $\boldsymbol{\psi}_{\mathrm{s}} = \psi_{\mathrm{s}\alpha} + j\psi_{\mathrm{s}\beta}$, and $\boldsymbol{\psi}_{\mathrm{r}} = \psi_{\mathrm{r}\alpha} + j\psi_{\mathrm{r}\beta}$. Based on (4), the instantaneous variation of stator current can be expressed in the $\alpha\beta$ reference frame as follows,

$$\begin{cases} \dfrac{\mathrm{d}i_{\mathrm{s}\alpha}}{\mathrm{d}t} = \dfrac{1}{\sigma L_{\mathrm{m}}}(v_{\mathrm{r}\alpha} - \dfrac{L_{\mathrm{r}}}{L_{\mathrm{m}}}v_{\mathrm{s}\alpha} - R_{\mathrm{r}}i_{\mathrm{r}\alpha} + \dfrac{R_{\mathrm{s}}L_{\mathrm{r}}}{L_{\mathrm{m}}}i_{\mathrm{s}\alpha} \\ \qquad - \omega_{\mathrm{e}}\dfrac{L_{\mathrm{r}}}{L_{\mathrm{m}}}\psi_{\mathrm{s}\beta} - \sigma\omega_{\mathrm{e}}L_{\mathrm{m}}i_{\mathrm{s}\beta}) \\ \dfrac{\mathrm{d}i_{\mathrm{s}\beta}}{dt} = \dfrac{1}{\sigma L_{\mathrm{m}}}(v_{\mathrm{r}\beta} - \dfrac{L_{\mathrm{r}}}{L_{\mathrm{m}}}v_{\mathrm{s}\beta} - R_{\mathrm{r}}i_{\mathrm{r}\beta} + \dfrac{R_{\mathrm{s}}L_{\mathrm{r}}}{L_{\mathrm{m}}}i_{\mathrm{s}\beta} \\ \qquad + \omega_{\mathrm{e}}\dfrac{L_{\mathrm{r}}}{L_{\mathrm{m}}}\psi_{\mathrm{s}\alpha} + \sigma\omega_{\mathrm{e}}L_{\mathrm{m}}i_{\mathrm{s}\alpha}) \end{cases} \tag{5}$$

The stator side active and reactive power are written as,

$$P_{\rm s}+jQ_{\rm s}=-\frac{3}{2}v_{\rm s}\cdot i_{\rm s}^{\rm s*} \tag{6}$$

By differentiating (6), the instantaneous variations of the stator active and reactive power are derived as follows,

$$\begin{cases}\dfrac{{\rm d}P_{\rm s}}{{\rm d}t}=-\dfrac{3}{2}(\dfrac{{\rm d}v_{{\rm s}\alpha}}{{\rm d}t}i_{{\rm s}\alpha}+\dfrac{{\rm d}i_{{\rm s}\alpha}}{{\rm d}t}v_{{\rm s}\alpha}+\dfrac{{\rm d}v_{{\rm s}\beta}}{{\rm d}t}i_{{\rm s}\beta}+\dfrac{{\rm d}i_{{\rm s}\beta}}{{\rm d}t}v_{{\rm s}\beta})\\ \dfrac{{\rm d}Q_{\rm s}}{{\rm d}t}=-\dfrac{3}{2}(\dfrac{{\rm d}v_{{\rm s}\beta}}{{\rm d}t}i_{{\rm s}\alpha}+\dfrac{{\rm d}i_{{\rm s}\alpha}}{{\rm d}t}v_{{\rm s}\beta}-\dfrac{{\rm d}v_{{\rm s}\alpha}}{{\rm d}t}i_{{\rm s}\beta}-\dfrac{{\rm d}i_{{\rm s}\beta}}{{\rm d}t}v_{{\rm s}\alpha})\end{cases} \tag{7}$$

In this paper, an ideal network with angular frequency $\omega_s$ is considered. Therefore, the stator voltage in the $\alpha\beta$ reference frame can be expressed as $v_{{\rm s}\alpha}=|v_{\rm s}|\cos(\omega_{\rm s}{\rm t}+\theta_0)$ and $v_{{\rm s}\beta}=|v_{\rm s}|\sin(\omega_{\rm s}{\rm t}+\theta_0)$. The instantaneous network voltage variations are obtained as,

$$\begin{cases}\dfrac{{\rm d}v_{{\rm s}\alpha}}{{\rm d}t}=-\omega_{\rm s}v_{{\rm s}\beta}\\ \dfrac{{\rm d}v_{{\rm s}\beta}}{{\rm d}t}=\omega_{\rm s}v_{{\rm s}\alpha}\end{cases} \tag{8}$$

The impact of stator resistance to the stator flux can be ignored and following can be obtained,

$$\boldsymbol{\psi}_{\rm s}=-j\frac{1}{\omega_s}\boldsymbol{v}_{\rm s} \tag{9}$$

By manipulating (5), (7), (8) and (9), the dynamics of instantaneous active and reactive power can be deduced,

$$\begin{cases}\dfrac{{\rm d}P_{\rm s}}{{\rm d}t}=-\omega_{\rm r}Q_{\rm s}+\dfrac{L_{\rm r}R_{\rm s}}{\sigma L_{\rm m}^2}P_{\rm s}-\dfrac{3}{2L_{\rm m}\sigma}[(v_{{\rm r}\alpha}v_{{\rm s}\alpha}+v_{{\rm r}\beta}v_{{\rm s}\beta})\\ \qquad -R_{\rm r}(i_{{\rm r}\alpha}v_{{\rm s}\alpha}+i_{{\rm r}\beta}v_{{\rm s}\beta})-\dfrac{L_{\rm r}\omega_{\rm r}}{L_{\rm m}\omega_{\rm s}}|v_{\rm s}|^2]\\ \dfrac{dQ_s}{dt}=\omega_{\rm r}P_{\rm s}+\dfrac{L_{\rm r}R_{\rm s}}{\sigma L_{\rm m}^2}Q_{\rm s}-\dfrac{3}{2L_{\rm m}\sigma}[(v_{r\alpha}v_{s\beta}-v_{r\beta}v_{s\alpha})\\ \qquad +R_{\rm r}(i_{r\beta}v_{s\alpha}-i_{r\alpha}v_{s\beta})]\end{cases} \tag{10}$$

The improved VM-DPC for RSC is designed based on the expression of instantaneous active and reactive power of RSC, which will be explained in the next section.

To build the model of GSC, the stator voltage $\boldsymbol{v}_{\rm s}$ is written in the $\alpha\beta$ reference frame in terms of the GSC input current $i_{\rm g}$ and the controlled converter terminal voltage $v_{\rm g}$ as follows,

$$\boldsymbol{v}_{\rm s}=R_{\rm g}\boldsymbol{i}_{\rm g}+L_{\rm g}\frac{d\boldsymbol{i}_{\rm g}}{dt}+\boldsymbol{v}_{\rm g} \tag{11}$$

where $L_{\rm g}$ and $R_{\rm g}$ are the inductance and resistance of GSC, respectively. The active and reactive power of the grid side converter can be written as $P_{\rm g}=\frac{3}{2}{\rm Re}(\boldsymbol{v}_{\rm g}\cdot\boldsymbol{i}_{\rm g})$ and $Q_{\rm g}=\frac{3}{2}{\rm Im}(\boldsymbol{v}_{\rm g}\cdot\boldsymbol{i}_{\rm g})$, respectively. The instantaneous variations of the GSC active and reactive power can be derived as,

$$\begin{cases}\dfrac{{\rm d}P_{\rm g}}{{\rm d}t}=\dfrac{3}{2}(\dfrac{{\rm d}v_{{\rm s}\alpha}}{{\rm d}t}i_{{\rm g}\alpha}+\dfrac{{\rm d}i_{{\rm g}\alpha}}{{\rm d}t}v_{{\rm s}\alpha}+\dfrac{{\rm d}v_{{\rm s}\beta}}{{\rm d}t}i_{{\rm g}\beta}+\dfrac{{\rm d}i_{{\rm g}\beta}}{{\rm d}t}v_{{\rm s}\beta})\\ \dfrac{{\rm d}Q_{\rm g}}{{\rm d}t}=\dfrac{3}{2}(\dfrac{{\rm d}v_{{\rm s}\beta}}{{\rm d}t}i_{{\rm g}\alpha}+\dfrac{{\rm d}i_{{\rm g}\alpha}}{{\rm d}t}v_{{\rm s}\beta}-\dfrac{{\rm d}v_{{\rm s}\alpha}}{{\rm d}t}i_{{\rm g}\beta}-\dfrac{{\rm d}i_{{\rm g}\beta}}{{\rm d}t}v_{{\rm s}\alpha})\end{cases} \tag{12}$$

By assuming a balanced grid voltage, the dynamics of the instantaneous active and reactive power of grid side converter in the $\alpha\beta$ reference frame are obtained by using (11) and (12) as follows,

$$\begin{cases}\dfrac{dP_{\rm g}}{dt}=-\dfrac{R_{\rm g}}{L_{\rm g}}P_{\rm g}-\omega_{\rm s}Q_{\rm g}+\dfrac{3}{2L_{\rm g}}(v_{{\rm s}\alpha}v_{{\rm g}\alpha}+v_{{\rm s}\beta}v_{{\rm g}\beta}-|\boldsymbol{v}_{\rm s}|^2)\\ \dfrac{dQ_{\rm g}}{dt}=-\dfrac{R_{\rm g}}{L_{\rm g}}Q_{\rm g}+\omega_{\rm s}P_{\rm g}+\dfrac{3}{2L_{\rm g}}(v_{{\rm s}\beta}v_{{\rm g}\alpha}-v_{{\rm s}\alpha}v_{{\rm g}\beta})\end{cases} \tag{13}$$

The expression of instantaneous power variations are used as the design basis of the GVM-DPC applied in the GSC.

## III. VM-DPC Design for The BTB Converter

### A. Rotor Side Controller Design

To achieve an LTI characteristic and introduce the structure of VM-DPC, Voltage Modulated Regulated (VMR) inputs are firstly defined as [27],

$$\begin{cases}U_{\rm rP}=v_{{\rm r}\alpha}v_{{\rm sf}\alpha}+v_{{\rm r}\beta}v_{{\rm sf}\beta}-\dfrac{L_{\rm r}\omega_{\rm r}}{L_{\rm m}\omega_{\rm s}}|\boldsymbol{v}_{\rm sf}|^2\\ U_{\rm rQ}=v_{{\rm r}\alpha}v_{{\rm sf}\beta}-v_{{\rm r}\beta}v_{{\rm sf}\alpha}\end{cases} \tag{14}$$

where $\boldsymbol{v}_{\rm sf}$ is defined as the input of VM-DPC. It can be assumed that $\boldsymbol{v}_{\rm sf}=\boldsymbol{v}_{\rm s}$ under ideal voltage condition. However, the harmonics are largely existed in the stator voltage when DFIG is connected with a weak-grid, which will affect the control performance. Therefore, to guarantee the performance of the controller under weak-grid, a band-pass filter (BPF) is generally used to obtain the value of stator voltage. The inputs can be distinguished from the actual stator voltage and expressed by $\boldsymbol{v}_{\rm sf}=G_{\rm f}\boldsymbol{v}_{\rm s}$. The voltage coupling terms in (10) can be replaced by the VMR inputs defined in (14) and the following is obtained,

$$\begin{aligned}U_{\rm rP}=&-k_{\rm s}\nu_{\rm rp}-\underbrace{k_{\rm s}\omega_{\rm r}Q_{\rm sf}}_{\rm feed-forward}+\underbrace{R_{\rm r}(v_{{\rm sf}\alpha}i_{{\rm r}\alpha}+v_{{\rm sf}\beta}i_{{\rm r}\beta})}_{\rm compensation\ term\ C_P}\\ U_{\rm rQ}=&-k_{\rm s}\nu_{\rm rq}+\underbrace{k_{\rm s}\omega_{\rm r}P_{\rm sf}}_{\rm feed-forward}+\underbrace{R_{\rm r}(v_{{\rm sf}\beta}i_{{\rm r}\alpha}-v_{{\rm sf}\alpha}i_{{\rm r}\beta})}_{\rm compensation\ term\ C_Q}\end{aligned} \tag{15}$$

where $k_{\rm s}=\frac{2\sigma L_{\rm m}}{3}$ is the proportional control coefficient, $P_{\rm sf}$ and $Q_{\rm sf}$ are the calculated power components based on $v_{\rm sf}$ and $i_{\rm s}$. $C_{\rm P}$ and $C_{\rm Q}$ are the feed-forward compensation terms representing the coupling between stator voltage and rotor current. The terms can be neglected in alternative since $R_{\rm r}$ is usually relatively small in the DFIG system with a large capacity, where it has little effect on the control performance. Therefore, the rotor side current measurement is not required and the control structure can be further simplified. In order to decouple the active and reactive power loop, the feed-forward compensation terms $k_{\rm s}\omega_{\rm r}Q_{\rm sf}$ and $k_{\rm s}\omega_{\rm r}P_{\rm sf}$ are designed for $U_{\rm rP}$ and $U_{\rm rQ}$, respectively. $\nu_{\rm rp}$ and $\nu_{\rm rq}$ are defined as the active and reactive power terms with their differential expression, which can be written as follows,

$$\begin{cases}\nu_{\rm rp}=\dfrac{{\rm d}P_{\rm sf}}{{\rm d}t}-\dfrac{L_{\rm r}R_{\rm s}}{\sigma L_{\rm m}^2}P_{\rm sf}\\ \nu_{\rm rq}=\dfrac{dQ_{\rm sf}}{dt}-\dfrac{L_{\rm r}R_{\rm s}}{\sigma L_{\rm m}^2}Q_{\rm sf}\end{cases} \tag{16}$$

Since there is no coupling between the active and reactive power, various control techniques can be chosen to generate $\nu_{\rm rp}$ and $\nu_{\rm rq}$. In this paper, a simple PI control is selected,

$$\begin{cases} \nu_{\rm rp} = K_{\rm rp}(P_{\rm s}^* - P_{\rm sf}) + K_{ri}\int (P_{\rm s}^* - P_{\rm sf})dt \\ \nu_{\rm rq} = K_{\rm rp}(Q_{\rm s}^* - Q_{\rm sf}) + K_{ri}\int (Q_{\rm s}^* - Q_{\rm sf})dt \end{cases} \tag{17}$$

where $P_{\rm s}^*$ and $Q_{\rm s}^*$ are the references of stator active and reactive powers, respectively. $K_{\rm rp}$, $K_{\rm ri}$ are the control parameters of the rotor side VM-DPC. To prevent the RSC from overcurrent, the reference value of the stator powers are limited by following relationship,

$$\begin{aligned} 0 \le & P_{\rm s}^* \le P_{\rm s,max} \\ Q_{\rm s,min} \le & Q_{\rm s}^* \le Q_{\rm s,max} \end{aligned} \tag{18}$$

where $P_{\rm s,max}$ is the maximum active power, $Q_{\rm s,min}$ and $Q_{\rm s,max}$ are the upper limit and lower limit of the reactive power, respectively. Assuming the $d$-axis is in the same direction as the stator flux and the resistance is small enough to be neglected, $P_{\rm sf}$ and $Q_{\rm sf}$ can be represented by the rotor current components in $dq$ reference frame as [35],

$$\begin{cases} P_{\rm sf} = \dfrac{3}{2}|v_{\rm sf}|\dfrac{L_{\rm m}}{L_{\rm s}}i_{\rm rq} \\ Q_{\rm sf} = \dfrac{3}{2}(|v_{\rm sf}|\dfrac{L_{\rm m}}{L_{\rm s}}i_{\rm rd} - \dfrac{|v_{\rm sf}^2|}{\omega_{\rm s}L_{\rm s}}) \end{cases} \tag{19}$$

Therefore, $P_{\rm s,max}$ can be calculated according to the magnitude of the maximum rotor current $i_{\rm r,max}$ and the magnitude of the measured stator voltage $|v_{\rm sf}|$ as,

$$P_{\rm s,max} = \frac{3}{2}|v_{\rm sf}|\frac{L_{\rm m}}{L_{\rm s}}\underbrace{(0.9i_{\rm r,max})}_{i_{\rm rq,max}} \tag{20}$$

The maximum rotor current component in $d$ axis is determined by the maximum rotor current $i_{\rm r,max}$ and the calculated real-time active power $P_{\rm sf}$ as follows,

$$i_{\rm rd,max} = \sqrt{i_{\rm r,max}^2 - (\frac{2L_{\rm s}P_{\rm sf}}{3L_{\rm m}|v_{\rm sf}|})^2} \tag{21}$$

Therefore, the limitation of $Q_{\rm s}$ can be set as,

$$\begin{aligned} Q_{\rm s,min} = & \frac{3}{2}(-|v_{\rm sf}|\frac{L_{\rm m}}{L_{\rm s}}(i_{\rm rd,max}) - \frac{|v_{\rm sf}^2|}{\omega_{\rm s}L_{\rm s}}) \\ Q_{\rm s,max} = & \frac{3}{2}(|v_{\rm sf}|\frac{L_{\rm m}}{L_{\rm s}}i_{\rm rd,max} - \frac{|v_{\rm sf}^2|}{\omega_{\rm s}L_{\rm s}}) \end{aligned} \tag{22}$$

Finally, by using the inversion of (14), the controlled rotor side voltage signal in the $\alpha\beta$ reference frame can be calculated as,

$$\begin{cases} v_{\rm r\alpha} = \dfrac{v_{\rm sf\alpha}U_{\rm rP} + v_{\rm sf\beta}U_{\rm rQ}}{|\boldsymbol{v}_{\rm sf}|^2} + \dfrac{L_{\rm r}\omega_{\rm r}}{L_{\rm m}\omega_{\rm s}}v_{\rm sf\alpha} \\ v_{\rm r\beta} = \dfrac{v_{\rm sf\beta}U_{\rm rP} - v_{\rm sf\alpha}U_{\rm rQ}}{|\boldsymbol{v}_{\rm sf}|^2} + \dfrac{L_{\rm r}\omega_{\rm r}}{L_{\rm m}\omega_{\rm s}}v_{\rm sf\beta} \end{cases} \tag{23}$$

The control inputs $v_{\rm r\alpha}$ and $v_{\rm r\beta}$ are transformed into the output switching signals by using the conventional SVPWM technique. The block control diagram of RSC is shown in Fig. 2.

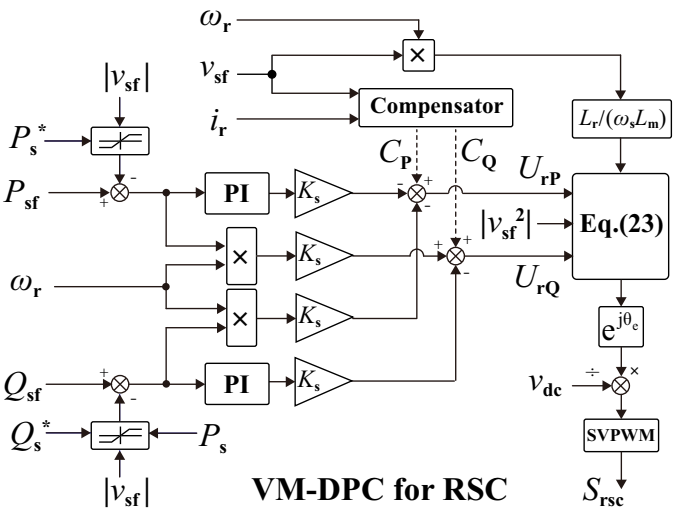


Fig. 2. Control system block diagram of RSC with proposed improved voltage-modulated direct power control (VM-DPC).

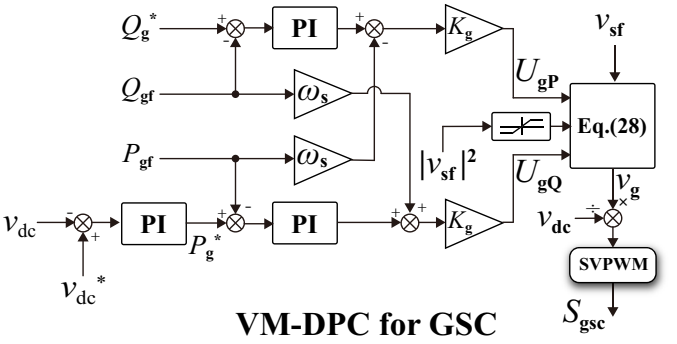


Fig. 3. Control system block diagram of GSC with voltage-modulated direct power control (VM-DPC).

### *B. Grid Side Controller Design*

The design of the grid side controller is also based on the concept of VM-DPC [24]. To transform the control of GSC into an LTI closed-loop system, the VMR inputs of GSC in (13) are defined as follows,

$$\begin{cases} U_{\rm gP} = v_{\rm sf\alpha}v_{\rm g\alpha} + v_{\rm sf\beta}v_{\rm g\beta} - |\boldsymbol{v}_{\rm s}|^2 \\ U_{\rm gQ} = v_{\rm sf\beta}v_{\rm g\alpha} - v_{\rm sf\alpha}v_{\rm g\beta} \end{cases} \tag{24}$$

By using the definition of VMR inputs, the coupling terms in (13) are replaced and the VMR inputs can be expressed in terms of the calculated power of GSC, i.e., $P_{\rm gf}$ and $Q_{\rm gf}$ as,

$$\begin{cases} U_{\rm gP} = k_{\rm g}\omega_{\rm s}Q_{\rm gf} + k_{\rm g}\underbrace{(\dfrac{dP_{\rm gf}}{dt} + \dfrac{R_{\rm g}}{L_{\rm g}}P_{\rm gf})}_{\nu_{\rm gp}} \\ U_{\rm gQ} = -k_{\rm g}\omega_{\rm s}P_{\rm gf} + k_{\rm g}\underbrace{(\dfrac{dQ_{\rm gf}}{dt} + \dfrac{R_{\rm g}}{L_{\rm g}}Q_{\rm gf})}_{\nu_{\rm gq}} \end{cases} \tag{25}$$

where $k_{\rm g} = \frac{2L_{\rm g}}{3}$ is the gain coefficient of the grid side controller. Feed-forward control is adopted to cancel the coupling between active and reactive power loops. $\nu_{\rm gp}, \nu_{\rm gq}$ are power

regulation terms of GSC. The PI controller of the inner loop of GSC side VM-DPC is chosen to have the same structure of RSC in (17) as follows,

$$\begin{cases} \nu_{\rm gp} = K_{\rm gp}(P_{\rm g}^* - P_{\rm gf}) + K_{gi}\int (P_{\rm g}^* - P_{\rm gf})dt \\ \nu_{\rm gq} = K_{\rm gp}(Q_{\rm g}^* - Q_{\rm gf}) + K_{gi}\int (Q_{\rm g}^* - Q_{\rm gf})dt \end{cases} \tag{26}$$

where $K_{\rm gp}$, $K_{\rm gi}$ are the control parameters. The power reference values are represented by $P_{\rm g}^*$ and $Q_{\rm g}^*$, respectively. The GSC is considered to operate at the unity power factor operation mode. The active power loop is used to maintain a constant dc-link voltage. The reactive power reference is set to 0, and the outer loop control is designed as,

$$P_{\rm g}^* = K_{\rm gp,dc}(v_{\rm dc}^* - v_{\rm dc}) + K_{\rm gi,dc}\int (v_{\rm dc}^* - v_{\rm dc})dt \tag{27}$$

Finally, by using the inversion expression of (24), the voltage regulation signals of GSC can be deduced as,

$$\begin{cases} v_{{\rm g}\alpha} = \dfrac{v_{{\rm sf}\alpha}U_{\rm gP} + v_{{\rm sf}\beta}U_{\rm gQ}}{|\boldsymbol{v}_{\rm sf}|^2} + v_{{\rm sf}\alpha} \\ v_{{\rm g}\beta} = \dfrac{v_{{\rm sf}\beta}U_{\rm gP} - v_{{\rm sf}\alpha}U_{\rm gQ}}{|\boldsymbol{v}_{\rm sf}|^2} + v_{{\rm sf}\beta} \end{cases} \tag{28}$$

Consequently, the controller of the GSC can be designed and represented by a block control diagram as shown in Fig. 3.

### C. Linear Time Invariant Characteristic

By differentiating the simultaneous equations of (16) and (17) and using the Laplace transform, the dynamics of RSC control can be represented by a second-order transfer function as follows,

$$\begin{cases} \dfrac{P_{\rm s}}{P_{\rm s}^*} = \dfrac{K_{\rm rp}s + K_{\rm ri}}{s^2 + (-\frac{R_{\rm s}L_{\rm r}}{\sigma L_{\rm m}^2} + K_{\rm rp})s + K_{\rm ri}} \\ \dfrac{Q_{\rm s}}{Q_{\rm s}^*} = \dfrac{K_{\rm rp}s + K_{\rm ri}}{s^2 + (-\frac{R_{\rm s}L_{\rm r}}{\sigma L_{\rm m}^2} + K_{\rm rp})s + K_{\rm ri}} \end{cases} \tag{29}$$

The closed-loop dynamics of the active and reactive powers are described by the polynomial of transfer functions (29) as follows,

$$s^2 + \underbrace{(-\frac{R_{\rm s}L_{\rm r}}{\sigma L_{\rm m}^2} + K_{\rm rp})}_{2\zeta\omega_{\rm n}} s + \underbrace{K_{\rm ri}}_{\omega_{\rm n}^2} = 0 \tag{30}$$

in which $\omega_n$ and $\zeta$ denote the natural frequency and damping factor, respectively. From the definition of $\sigma$, it can easily be deduced that $\sigma < 0$, if the PI parameters $K_{\rm rp}$, $K_{\rm rp}$ are designed as positive values, $\zeta\omega_{\rm n} > 0$, according to linear analysis method, the closed-loop system with the proposed method is globally exponentially stable [27], [34].

## IV. Stability Analysis

It should be noted that the grid impedance strongly affects the stability of the grid-connected DFIG system. Consequently, in this section, the stability analysis of the DFIG with the proposed method considering the grid impedance is investigated.

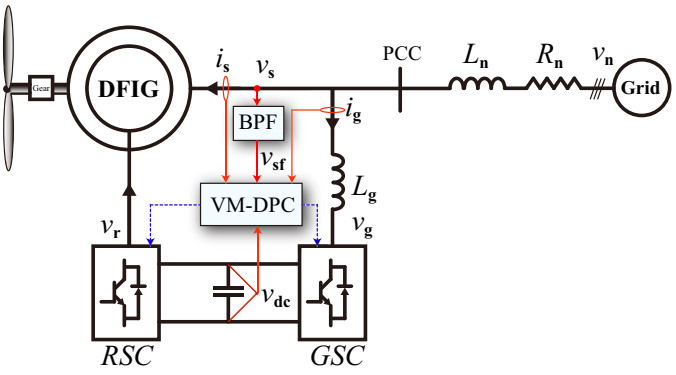


Fig. 4. Scheme of grid-connected DFIG using VM-DPC.

A general diagram of the grid-connected DFIG is shown in Fig. 4, where $R_{\rm n}$ and $L_{\rm n}$ are the equivalent grid resistance and inductance, respectively.

The short circuit ratio (SCR) is defined by the ratio of the short-circuit capacity of the system at the point of common coupling to the rated power of the equipment, such as SCR$=S_{\rm sc}/S_{\rm n}$, [36], [37], which is calculated as,

$$\mathrm{SCR} = \frac{\mathrm{V}_{\rm s,nom}^2}{\mathrm{P}_{\rm s,nom}|\mathrm{Z_n}|} \tag{31}$$

where $v_{\rm s,nom}$ is the nominal voltage at PCC, $P_{\rm s,nom} = P_{\rm s}^*$ is the rated power of DFIG, $\boldsymbol{Z}_{\rm n} = R_{\rm n} + j\omega_{\rm s}L_{\rm n}$ denotes the total grid impedance. In this section, an eigenvalue analysis of the RSC with proposed VM-DPC is presented. The stability of the GSC could be referred from [27], where the stability for the GSC with the VM-DPC under a weak-grid condition is investigated. To guarantee the control performance of DFIG using VM-DPC under weak-grid condition, a BPF is used to remove the harmonics and obtain the fundamental component of the measured voltage. The transfer function of the BPF can be expressed as follows,

$$\boldsymbol{v}_{\rm sf} = \underbrace{\frac{2\zeta\omega_{\rm s}s}{s^2 + 2\zeta\omega_{\rm s}s + \omega_{\rm s}^2}}_{G_{\rm f}}\boldsymbol{v}_{\rm s} \tag{32}$$

where $v_{\rm s,m}$ is the measured voltage at PCC, $\boldsymbol{v}_{\rm s}$ is the output of BPF. In order to consider the dynamics of the BPF, the new state of the system $\boldsymbol{x} \in \mathbb{R}^6$ is defined as, $\boldsymbol{x} = [i_{{\rm s}\alpha}, i_{{\rm s}\beta}, x_\alpha, x_\beta, \dot{x_\alpha}, \dot{x_\beta}]^T$, where the deviations of the state variable $[x_\alpha, x_\beta, \dot{x_\alpha}, \dot{x_\beta}]$ can be expressed as, $[\dot{x_\alpha}, \dot{x_\beta}, \ddot{x_\alpha}, \ddot{x_\beta}] = [v_{{\rm sf}\alpha}, v_{{\rm sf}\beta}, \dot{v_{{\rm sf}\alpha}}, \dot{v_{{\rm sf}\beta}}]$. The voltage at PCC is the input of the controller, $\boldsymbol{v}_{\rm s} = [v_{{\rm s}\alpha}, v_{{\rm s}\beta}]^T \in \mathbb{R}^2$.

By substituting (15), (23) and (32) into (5), the system

dynamics can be obtained as follows,

$$\begin{bmatrix} \dot{i}_{s\alpha} \\ \dot{i}_{s\beta} \\ \dot{x}_{\alpha} \\ \dot{x}_{\beta} \\ \dot{x}_{\alpha} \\ \dot{x}_{\beta} \end{bmatrix} = \underbrace{\begin{bmatrix} A_{11} & A_{12} & 0 & 0 & A_{15} & A_{16} \\ A_{21} & A_{22} & 0 & 0 & A_{25} & A_{26} \\ 0 & 0 & 0 & 0 & 1 & 0 \\ 0 & 0 & 0 & 0 & 0 & 1 \\ 0 & 0 & -\omega_s & 0 & -2\zeta\omega_s & 0 \\ 0 & 0 & 0 & -\omega_s & 0 & -2\zeta\omega_s \end{bmatrix}}_{\boldsymbol{A}} \begin{bmatrix} i_{s\alpha} \\ i_{s\beta} \\ x_{\alpha} \\ x_{\beta} \\ \dot{x}_{\alpha} \\ \dot{x}_{\beta} \end{bmatrix} + \underbrace{\begin{bmatrix} B_{11} & 0 & 0 & 0 & 2\zeta\omega_s & 0 \\ 0 & B_{22} & 0 & 0 & 0 & 2\zeta\omega_s \end{bmatrix}^{\mathrm{T}}}_{\boldsymbol{B}} \begin{bmatrix} v_{s\alpha} \\ v_{s\beta} \end{bmatrix} \tag{33}$$

where the matrix parameters are,

$$\begin{aligned} A_{11} &= A_{22} = \frac{1}{\sigma L_m}\left(\frac{R_s L_r}{L_m} - \frac{3k_s K_{rp}}{2}\right) \\ A_{12} &= -A_{21} = \frac{1}{\sigma L_m}\left(-\sigma L_m \omega_e - \frac{3k_s \omega_r}{2}\right) \\ A_{15} &= A_{26} = \frac{1}{\sigma L_m}\left(-\frac{k_s K_{rp} P_s^*}{v_{s,ss}^2} + \frac{L_r \omega_r}{L_m \omega_s}\right) \\ A_{16} &= -A_{25} = \frac{1}{\sigma L_m}\left(-\frac{k_s K_{rp} Q_s^*}{v_{s,ss}^2}\right) \\ B_{11} &= B_{22} = -\frac{1}{\sigma L_m}\left(\frac{L_r \omega_r}{L_m \omega_s}\right) \end{aligned} \tag{34}$$

Note that the term $\boldsymbol{v}_{sf}^2$ is a dc value and the dynamics is comparatively slow [30]. Therefore, the dynamics of $\boldsymbol{v}_{sf}^2$ is not considered in (33), i.e., $|\boldsymbol{v}_{sf}|^2 = v_{s,ss}^2$, where $v_{s,ss}^2$ denotes the squared value of the stator voltage magnitude under steady-state. For the sake of the simplicity, only proportional controller in (17) is considered for the stability analysis in this paper. The dynamic equation consisting of $\boldsymbol{v}_s$, $\boldsymbol{i}_s$ and the grid voltage $\boldsymbol{v}_n$ is expressed as follows,

$$\boldsymbol{v}_s = \boldsymbol{L}_n \dot{\boldsymbol{x}} + \boldsymbol{R}_n \boldsymbol{x} + \boldsymbol{I}_2 \boldsymbol{v}_n \tag{35}$$

where $\boldsymbol{L}_n$, $\boldsymbol{R}_n$, and $\boldsymbol{I}_2$ are the transfer matrices, which can be written as, $\boldsymbol{L}_n = \begin{bmatrix} L_n & 0 & 0 & 0 & 0 & 0 \\ 0 & L_n & 0 & 0 & 0 & 0 \end{bmatrix}$, $\boldsymbol{R}_n = \begin{bmatrix} R_n & 0 & 0 & 0 & 0 & 0 \\ 0 & R_n & 0 & 0 & 0 & 0 \end{bmatrix}$, and $\boldsymbol{I}_2 = \begin{bmatrix} 1 & 0 \\ 0 & 1 \end{bmatrix}$, respectively. The grid voltage input of the system is, $\boldsymbol{v}_n = [v_{n\alpha}, v_{n\beta}]^T \in \mathbb{R}^2$. By substituting (35) into (33), the state-space model of the closed-loop system is finally expressed as,

$$\dot{\boldsymbol{x}} = (\boldsymbol{I}_6 - \boldsymbol{B}\boldsymbol{L}_n)^{-1}(\boldsymbol{A} + \boldsymbol{B}\boldsymbol{R}_n)\boldsymbol{x} + (\boldsymbol{I}_6 - \boldsymbol{B}\boldsymbol{L}_n)^{-1}\boldsymbol{B}\boldsymbol{v}_n \tag{36}$$

where $\boldsymbol{I}_6$ is a 6×6 identity matrix. In this paper, the rated power of DFIG is considered as, $P_{s,nom} = 1.5$ MW. The DFIG is set to operate in unity power factor mode. Moreover, the $X_n/R_n$ ratio is set to 9. The detailed parameters of the system are listed in Table. I.

Fig. 5 shows the eigenvalues of the closed-loop system with different BPF damping ratio ($\zeta = 0.1, \zeta = 0.707$). It can be observed that the eigenvalues moves to the imaginary axis when SCR decreases, which indicates that the system tends to become unstable. Moreover, the decreasing of $\zeta$ greatly changes the distribution of the eigenvalues near imaginary axis, the eigenvalues moves close to the imaginary axis when $\zeta$ decreases. But in general, the eigenvalues are located in the left half-plane, which indicates that the system with the proposed method remains stable under different grid conditions. It is noted that the maximum active output power of the wind turbine under unity power factor is limited in a weak grid as described in [37],

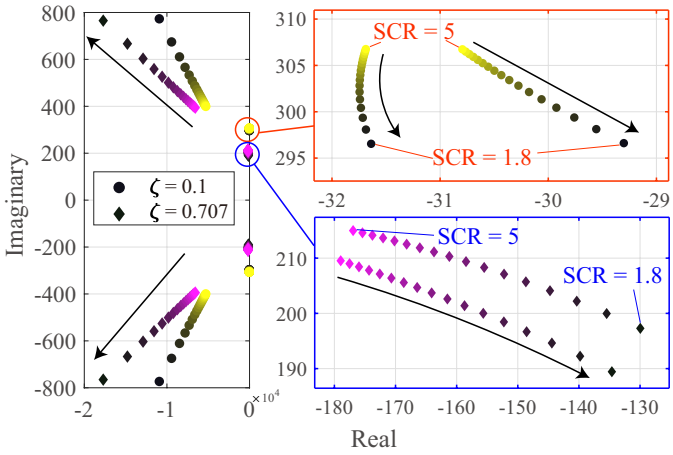


Fig. 5. Eigenvalues of the RSC closed-loop system with different BPF damping ratio when the SCR is changed from 5 to 1.8.

$$P_{s,max} = \frac{1}{2} \cdot \frac{1}{1 - \frac{1}{1+(X_n/R_n)^2}} \cdot \frac{v_n^2}{|\boldsymbol{Z}_n|} \tag{37}$$

According to (31) and (37), if the maximum active power is considered equal to the rated power, i.e., $P_{s,max} = P_{s,nom} = 1.5$ MW, then, the minimum SCR value can be calculated as $SCR_{min} = 1.61$ when the DFIG is operating in unity power factor mode. If SCR $< 1.61$, to keep the system stable, the reactive power needs to be injected into the grid [30], [37]. Another stability analysis method is based on the impedance model [10]. The dynamics of the system can also be further studied based on the distribution of the eigenvalues. Moreover, the impedance stability analysis of the grid-connected DFIG with the proposed VM-DPC will be studied in future research work.

## V. Simulation Results

A simulation model of a specific 1.5 MW DFIG system is studied in this paper. The RSC and GSC controllers are implemented by using Matlab/Simulink Simscape Power System. The simulation step is set to 5 $\mu$s, and the sampling frequency is set to 4 kHz during the simulation process. The DFIG is set to operate at constant rotor speed (1200 rpm, $\omega_e = 251.3$ rad/s). The GSC is mainly used to support the capacitor to build up a constant dc-link voltage at 1150 V, and ensure the bi-directional power flow through the GSC. The details of the parameters of the simulation system are shown in Table I, which is close to the real DFIG system [38].

### A. Steady-state Performance and Transient Response of Proposed VM-DPC

In this subsection, the steady-state and transient response of the DFIG system using the proposed VM-DPC is compared

TABLE I
PARAMETERS OF THE STUDIED 2 MW DFIG SYSTEM

| Parameter | Symbol | Value | Unit |
|---|---|---|---|
| Rated power | $P_{\mathrm{s}}^{*}$ | 1.5 | MW |
| Line-to-line voltage | $v_{\mathrm{s,rms}}$ | 690 | V |
| dc voltage | $v_{\mathrm{dc}}^{*}$ | 1150 | V |
| dc capacitor | $C_{\mathrm{dc}}$ | 0.08 | F |
| Sampling frequency | $f_{\mathrm{a}}$ | 4 | kHz |
| Switching frequency | $f_{\mathrm{w}}$ | 4 | kHz |
| Electrical angular speed | $\omega_{\mathrm{e}}$ | 251 | rad/s |
| System frequency | $f$ | 50 | Hz |
| Stator resistance | $R_{\mathrm{s}}$ | 2.6 | mΩ |
| Stator inductance | $L_{\mathrm{s}}$ | 2.6 | mH |
| Rotor resistance | $R_{\mathrm{r}}$ | 2.9 | mΩ |
| Rotor inductance | $L_{\mathrm{r}}$ | 2.6 | mH |
| Mutual inductance | $L_{\mathrm{m}}$ | 2.5 | mH |
| GSC resistance | $R_{\mathrm{g}}$ | 0.2 | mΩ |
| GSC inductance | $L_{\mathrm{g}}$ | 0.4 | mH |
| Grid resistance | $R_{\mathrm{n}}$ | 8 | mΩ |
| Grid inductance | $L_{\mathrm{n}}$ | 0.22 | mH |
| Grid capacitance | $C_{\mathrm{n}}$ | 50 | $\mu$F |
| Rotor current limitation | $i_{\mathrm{r,max}}$ | 2.22 | kA |
| Turns ratio | $u$ | 3 | |
| PI control parameters | | | |
| Parameter | Value | Parameter | Value |
| $K_{\mathrm{rp}}$ | 4000 | $K_{\mathrm{ri}}$ | 20000 |
| $K_{\mathrm{gp}}$ | 3750 | $K_{\mathrm{gi}}$ | 18750 |
| $K_{\mathrm{gp,dc}}$ | -1000 | $K_{\mathrm{gi,dc}}$ | -60000 |
| $k_{\mathrm{s}}$ | -0.000118 | $\zeta$ | 0.1 |

with a classical VOC which was originally designed in [39], also a SMC-DPC proposed in [22], and C-DPC [17]. The bandwidth of VM-DPC is designed to 628 Hz, which is calculated according to (29), and the bandwidth of the inner current loop of VOC is set to 644 Hz. It is noted that the BPF is not used in this comparative study. The stator active power reference and reactive power reference are set to 1.5 MW and 0 MVar respectively, at the beginning of the simulation. Two reference steps $\Delta P_{\mathrm{s}}^{*} = -0.75$ MW and $\Delta Q_{\mathrm{s}}^{*} = 0.75$ MVar are set at 3 s and 3.2 s separately to test the transient dynamics along with the coupling between the active and reactive power control loops. Fig. 6 shows the power and electromagnetic torque performance of four different control strategies at the power reference step. The results show the three DPC methods have faster transient response than the classical VOC with no overshoot at either the active and reactive power reference steps. The SMC-DPC induces power pulsations. The enlarged window of the reactive power reference step also shows the VM-DPC has the smallest interaction between the variations of active and reactive power among three DPC techniques. The differences between the steady-state electromagnetic torque performance of the four studied methods are not apparent.

Fig. 7 shows an enlarged window of stator current performance at the active power step between 2.98 s to 3.02 s. The results show that the steady-state performance of the VOC, C-DPC, and VM-DPC are satisfied. A comparison of the total harmonic distortion (THD) of the stator current with four different control techniques are shown in Fig. 8. The VOC, C-DPC, and the proposed improved VM-DPC achieve a stator current THD of about 1.4%, which indicates they have the same level of steady-state performance. The

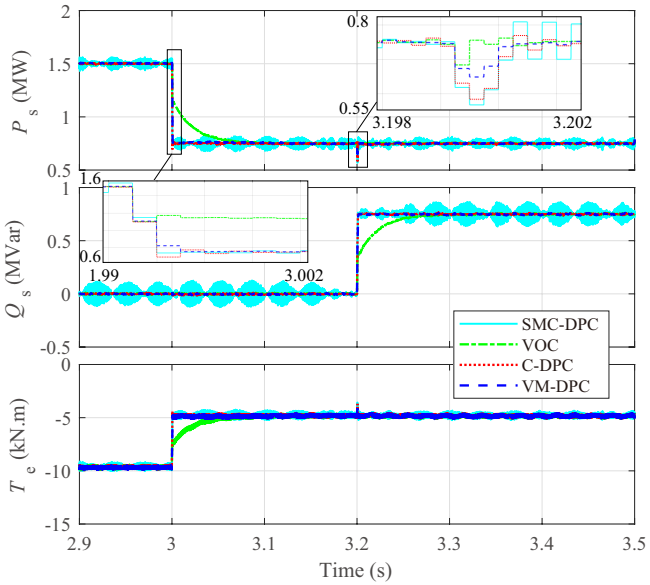


Fig. 6. Comparison of the transient performance of the active, reactive power and electromagnetic torque $T_{\mathrm{e}}$ at power reference step among the SMC-DPC, the classical VOC, the C-DPC and the proposed improved VM-DPC.

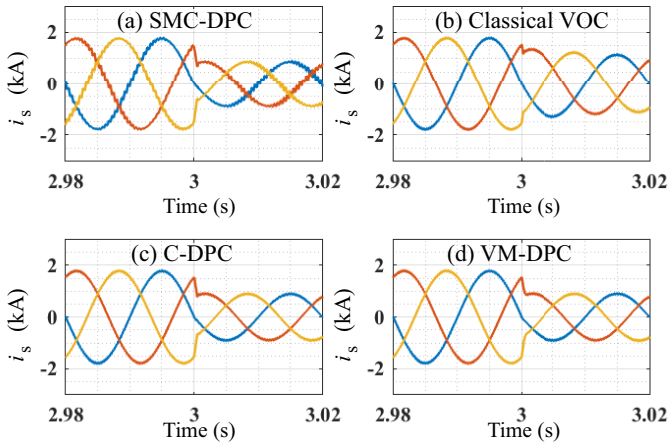


Fig. 7. Comparison of stator current response at transient power reference step among various control strategies.

SMC-DPC generates more stator current harmonics with a frequency around 2000 Hz. A comparison of the rotor current is presented in Fig. 9. It can be observed that the VM-DPC also manifests an excellent rotor current performance.

Detailed information about the comparison between four different methods is given in Table. II. The convergence time is considered to be the time spend of actual power value enter the 5% error band. The three DPC control techniques have approximately the same convergence time of about 1 ms, which is much lower than VOC. The THD of the VOC, C-DPC, and VM-DPC are around 1.4%, which indicate the three different methods have the same level of steady-state performance. The THD of SMC-DPC is 3.37%, which is the highest among the four control techniques. The decoupling effect between active and reactive power loops can be represented by the deviation rate of the active power when the reactive power reference value steps. The decoupling effect of four control strategies

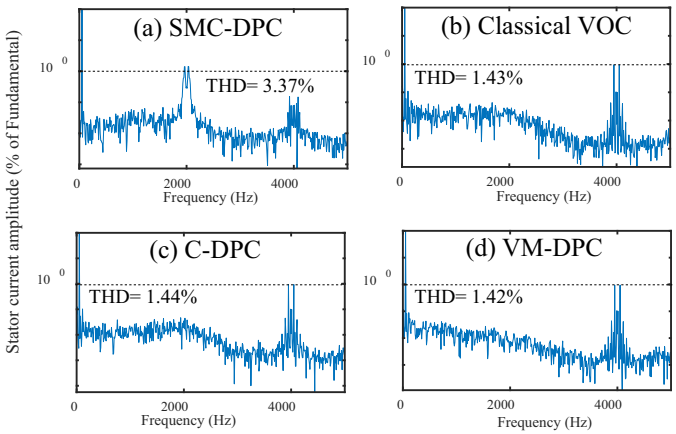


Fig. 8. Harmonic spectrum of stator output current in steady-state ($P_{\rm s} = 1.5$ MW, $Q_{\rm s} = 0$ Mvar).

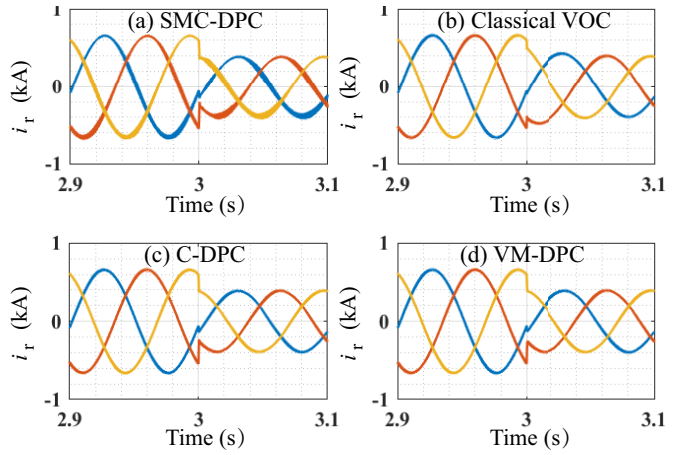


Fig. 9. Comparison of rotor current response at transient power reference step among various control strategies.

are compared as shown in the enlarged window of Fig. 6 and Table II. The results show that the VM-DPC has the second smallest deviation of about 6.7%, after the VOC method. Therefore, the effectiveness of the feed-forward compensation terms in the proposed VM-DPC is verified. Please note that the SMC-DPC and VM-DPC are directly built in the $\alpha\beta$ reference frame. Therefore, the structures of SMC-DPC and VM-DPC are simpler than that of VOC and C-DPC, which requires a voltage phase signal for coordinate transformation. Consequently, the results show that the VM-DPC is applicable in the high power DFIG system.

TABLE II
TRANSIENT AND STEADY-STATE PERFORMANCE WITH DIFFERENT CONTROL TECHNIQUES

| Method | Performance | | | Structure |
|---|---|---|---|---|
| | Convergence time | THD | Deviation rate | PLL and Coordinates |
| SMC-DPC | $\approx$ 1 ms | 3.37% | 12.0% | Not required ($\alpha\beta$) |
| VOC | $\approx$ 100 ms | 1.44% | 4.2% | Required ($dq$) |
| C-DPC | $\approx$ 1 ms | 1.43% | 10.5% | Virtual PLL ($dq$) |
| VM-DPC | $\approx$ 1 ms | 1.42% | 6.7% | Not required ($\alpha\beta$) |

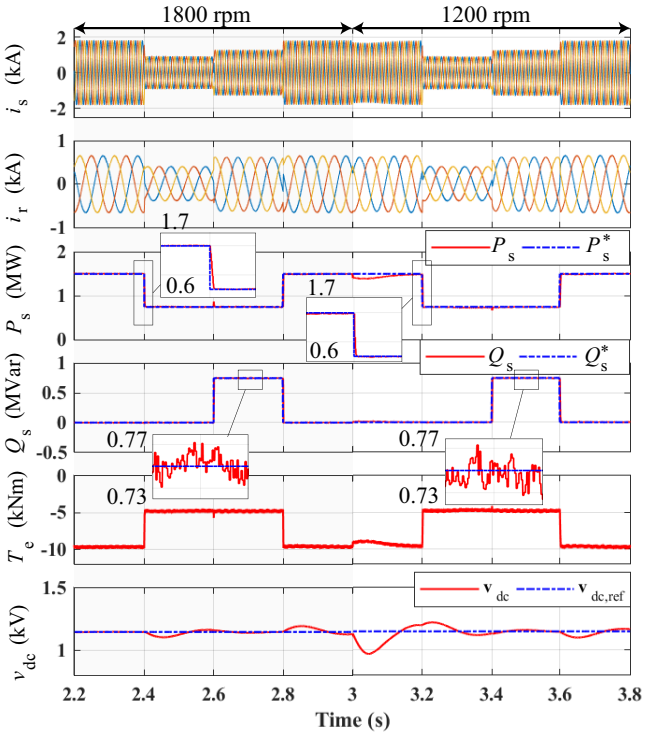


Fig. 10. Performance of DFIG using the proposed VM-DPC under different rotor speeds.

### B. Performance of VM-DPC Under Different Rotor Speed

In order to test the control performance of the proposed VM-DPC at different rotor speeds, a simulation is carried out as shown in Fig. 10. The rotor speed changes from 1800 rpm ($\omega_{\rm e}$ =377 rad/s) to 1200 rpm ($\omega_{\rm e}$ =235.6 rad/s) at 3 s. In order to compare the system performance at two different rotor speed. The steps of active power reference value $\Delta P_{\rm s}^* = -0.75$ MW are given at 2.4 s and 3.2 s, respectively. Also, the steps of reactive power reference value $\Delta Q_{\rm s}^* = 0.75$ MVar are set at 2.6 s and 3.4 s, respectively.

From the enlarged window of active and reactive power dynamics, it is observed that both transient response and steady-state performance of the proposed method are not affected by the variation of rotor speed. The transient dynamics of dc voltage at 3s is caused by the direction change of the power flow on the GSC side due to the variation of rotor speed.

### C. Robustness to Parameter Variation

Since there are many compensation terms in the proposed VM-DPC strategy and the values are closely related to the parameters of the generator, such as rotor resistance and mutual inductance, these parameters are difficult to be measured and may change over time because of the aging of devices and temperature variation. Therefore, to check the robustness against the parameters mismatch of the proposed VM-DPC, the mutual inductance $L_{\rm m}$ and rotor resistance $R_{\rm r}$ of the control parameters are increased by 30% at 3 s. The power reference steps are set as the same to Fig. 10. The simulation

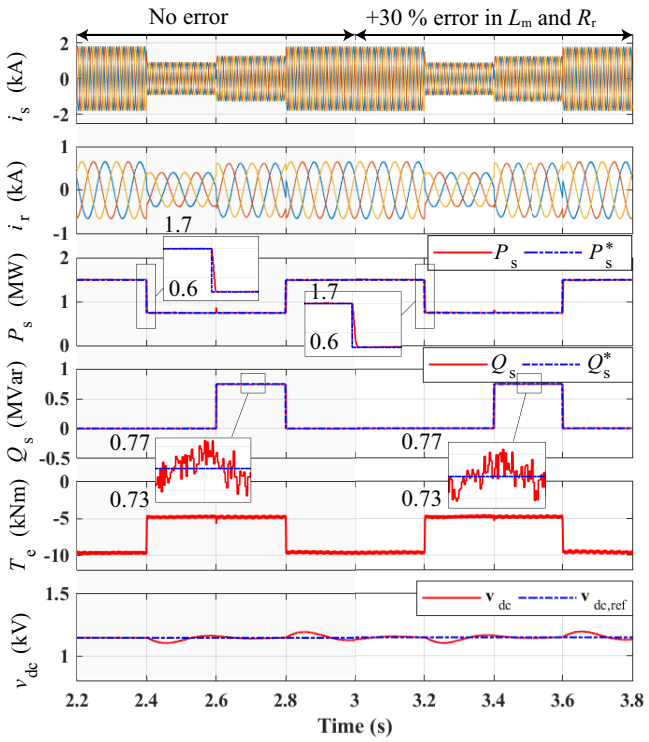


Fig. 11. Performance of DFIG using the proposed VM-DPC with $+30\%L_{\mathrm{m}}$ and $+30\%R_{\mathrm{r}}$ errors.

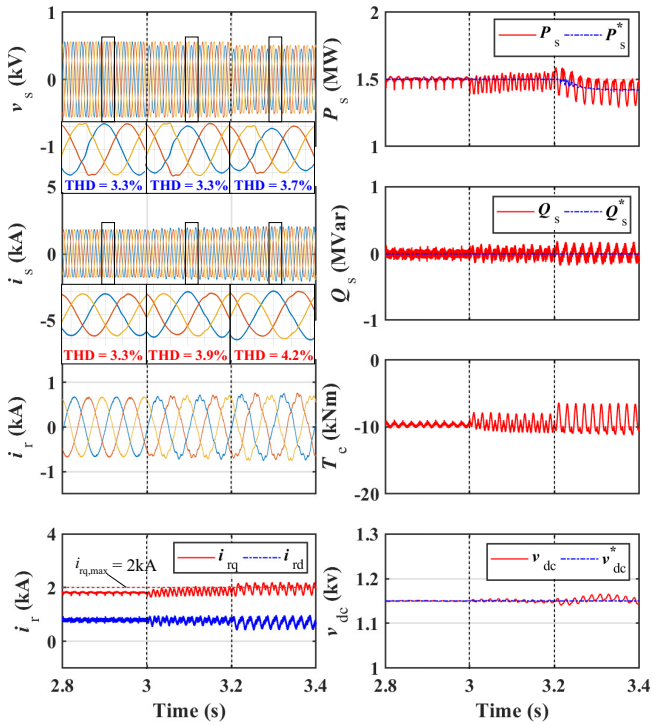


Fig. 12. Performance of DFIG using the proposed VM-DPC under harmonic distorted and unbalanced voltage dip conditions.

results presented in Fig. 11 confirm the good steady-state operation and fast transient response of the VM-DPC under $+30\%$ parameter variation. Consequently, it is concluded that the proposed VM-DPC has a robust property to parameter variations.

### *D. Performance Under Harmonic Distorted and grid fault Conditions*

In this subsection, the performance of the proposed method under distorted and unbalanced grid condition is tested. Since the accuracy of the control design depends on a non-distorted grid condition as presented in (8) and (9). The performance of DFIG using the VM-DPC under different voltage conditions is shown in Fig. 12, where the enlarged windows present the detailed waveforms of the stator voltage and currents. At first, DFIG is operated at a distorted grid, where the THD of the grid voltage is 3.3%. The results indicate the DFIG can maintain a steady-state performance with the current THD = 3.3%. At 3 s, a Phase-A voltage drop (0.9 p.u.) is set, and it excites the unbalanced components of stator currents and increase the current THD from 3.3% to 3.9%. Afterwards, at 3.2 s, the Phase-A voltage drops to 0.8 p.u and the phase-B, phase-C stator voltage drop to 0.9 p.u. It can be seen that the voltage dip introduces power ripples and increases the stator current harmonics from 3.9% to 4.2%. Moreover, from 3.2 s, the maximum active power ripples increase to 0.13 p.u, and the maximum electromagnetic torque ripples increase to 0.46 p.u. It can be seen that such unbalanced or distorted grid will slightly affect the performance, but the current THD is still below the range of the requirement [40]. In addition, it should be noted that the active power reference value drops to 1.3 MW after 3.2 s, which is caused by the limitation of the maximum rotor side currents. Furthermore, The performance of the proposed VM-DPC under severe voltage conditions is compared with conventional VOC as presented in Fig. 13, where a severe three-phase voltage drop (0.1 p.u.) is set at 2 s. It can be observed that the stator and rotor side currents are deformed, which are caused by the transient stator flux introduced by the grid fault. The proposed VM-DPC has a similar transient performance to the conventional VOC. The decaying process of the transient stator flux can be accelerated by the DPC based demagnetizing method proposed in [41]. The active power reference value $P_{\mathrm{s}}^*$ is decreased to 0.16 MW when the fault occurs, which verifies the proposed over-current protection algorithm.

Consequently, it is concluded that the DFIG controlled by the VM-DPC can operate under slight grid faults. The performance VM-DPC will be further improved to handle the severe unbalanced voltage drop conditions in future research works.

### *E. Performance Under Different Grid Parameters*

The performance of DFIG with the proposed VM-DPC under the grid condition with different SCR values are tested as shown in Fig. 14. The damping ratio of the BPF is set to $\zeta = 0.1$. The DFIG is connected with a stiff grid from the beginning of the simulation. At 3 s, an inductance $L_{\mathrm{n}} = 0.22$ mH and a resistance $R_{\mathrm{n}} = 8$ m$\Omega$ are added in series into the

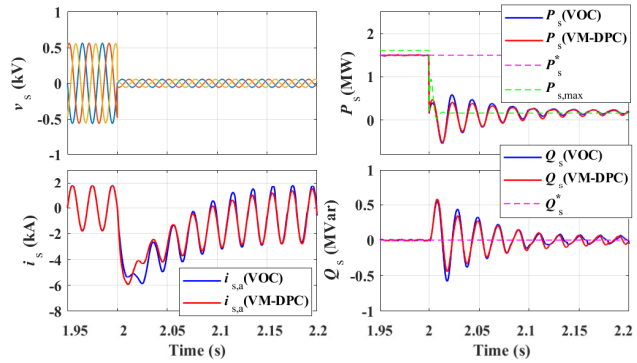


Fig. 13. Comparison of the performance under severe voltage drop conditions (0.1 p.u.) between conventional VOC and the proposed VM-DPC.

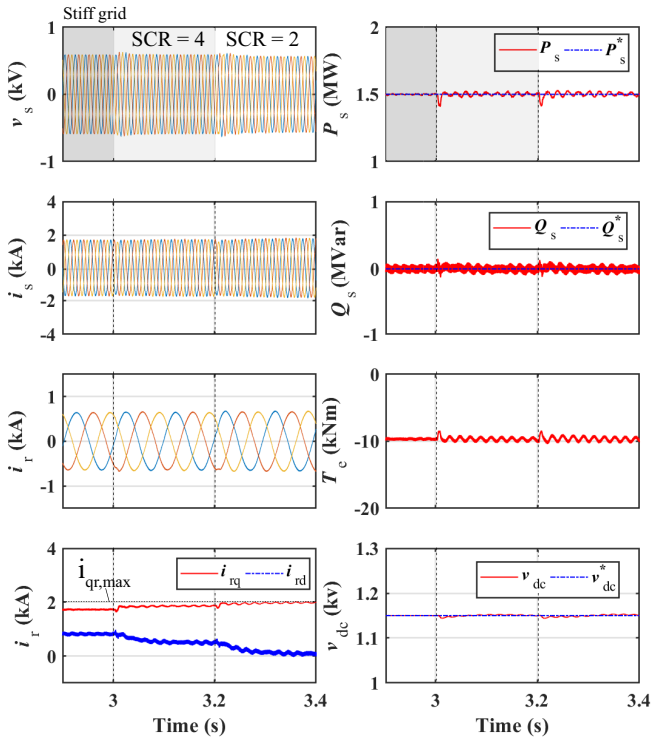


Fig. 14. Performance of DFIG using the proposed method in different grid impedance conditions.

grid, which make SCR = 4. Then, the SCR value is further decreased from 4 to 2 at 3.5 s. It is observed from Fig. 14 that the proposed VM-DPC controlled DFIG is stable and works well in different grid conditions. The results show consistency with the conclusions drawn in Section IV.

### *F. Discussion*

In this section, the performance of the DFIG using the proposed VM-DPC is tested in the different conditions. A comparison of the stator current THD manifests the proposed VM-DPC has the same level of steady-state performance as the VOC under a similar control bandwidth. Besides, the VM-DPC also features a fast transient response under different rotor speeds. The simulation results show also that the DFIG using the proposed method works well in the weak-grid

TABLE III
PARAMETERS OF EXPERIMENTAL DFIG PROTOTYPE

| Parameter | Symbol | Value | Unit |
|---|---|---|---|
| Rated power | $P^*_s$ | 7.5 | kW |
| Line-to-line voltage | $v_{s,rms}$ | 380 | V |
| dc voltage | $v^*_{dc}$ | 650 | V |
| dc capacitor | $C_{dc}$ | 600 | $\mu$F |
| System frequency | $f$ | 50 | Hz |
| Sampling frequency | $f_a$ | 10 | kHz |
| Switching frequency | $f_w$ | 10 | kHz |
| Stator resistance | $R_s$ | 0.44 | Ω |
| Stator inductance | $L_s$ | 82.7 | mH |
| Rotor resistance | $R_r$ | 0.64 | Ω |
| Rotor inductance | $L_r$ | 84.6 | mH |
| Mutual inductance | $L_m$ | 79.3 | mH |
| GSC inductance | $L_g$ | 18 | mH |
| Control Parameters | | | |
| Parameter | Value | Parameter | Value |
| $K_{rp}$ | 20000 | $K_{ri}$ | 100000 |
| $K_{gp}$ | 4500 | $K_{gi}$ | 20000 |
| $K_{gp,dc}$ | -10 | $K_{gi,dc}$ | -1000 |
| $k_s$ | -0.0059 | | |

conditions. Moreover, the proposed method features robustness against the generator parameter variations and the non-ideal voltage conditions. However, the performance of the DFIG using the proposed VM-DPC is susceptible to the unbalanced voltage dip conditions. Such grid faults will increase the stator current harmonics and cause ripples in the powers and the electromagnetic torque. It is noted that for the most of the DPC methods, the unbalanced voltage will introduce the negative-sequence components and third order harmonics in the stator currents, which affect the steady-state performance [12], [15], [23]. The problem can be solved by adding the compensation terms in the control loops as discussed in [15], [23]. However, these methods require further discussions about the relation of negative-sequence electromagnetic components of the DFIG under unbalanced voltage conditions, which are out of the scope of the paper. A voltage dip fault will result in natural flux in the stator side and cause a rotor side over-voltage [41]. In the extreme cases, such a phenomenon may even destroy the converter if not properly protected. The Low-Voltage-Ride-Through (LVRT) capability of the DFIG using DPC can be improved by using a stator natural flux cancellation technique [41]. The improvement of LVRT capability of the proposed method will be research in the future.

## VI. EXPERIMENTAL VALIDATION

In order to verify the effectiveness of the proposed VM-DPC, a prototype experimental setup, as shown in Fig. 15 is used. The experimental setup is composed of a 7.5 kW DFIG, which is connected with a speed-controlled induction machine operating at 1200 rpm. The capacity of the GSC and RSC is 5 kW and 7.5 kW, respectively. The GSC is mainly used to support the capacitor to operate at a constant dc-link voltage at 650 V. The switching frequency of two converters is both 10 kHz as well as sampling frequency. The control schemes are implemented in the DS1006 dSPACE system. The switching signal of GSC and RSC are generated by using the DS5101 digital waveform output board. The

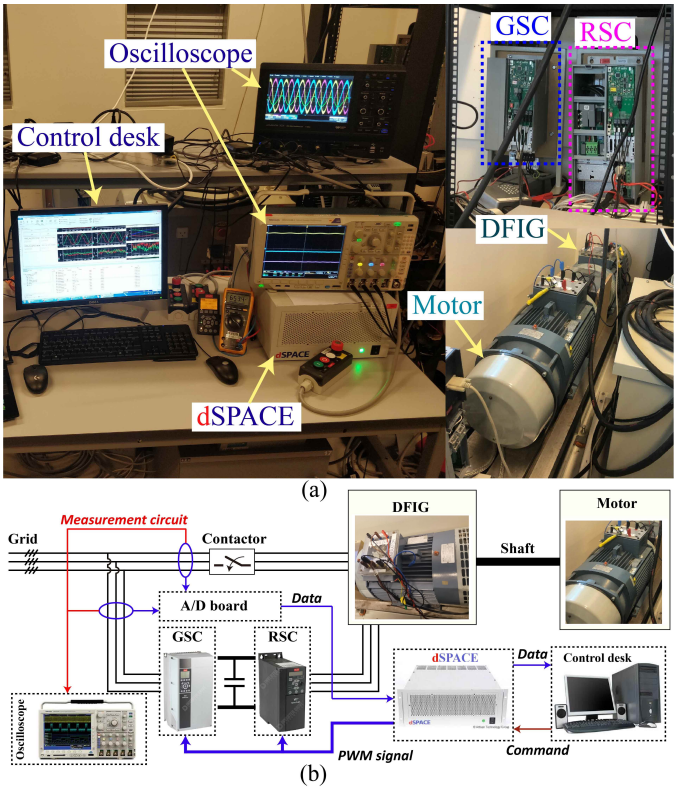


Fig. 15. Experimental setup to test DFIG with the proposed VM-DPC and VOC using dSPACE. (a) Photo. (b) Generic used system architecture.

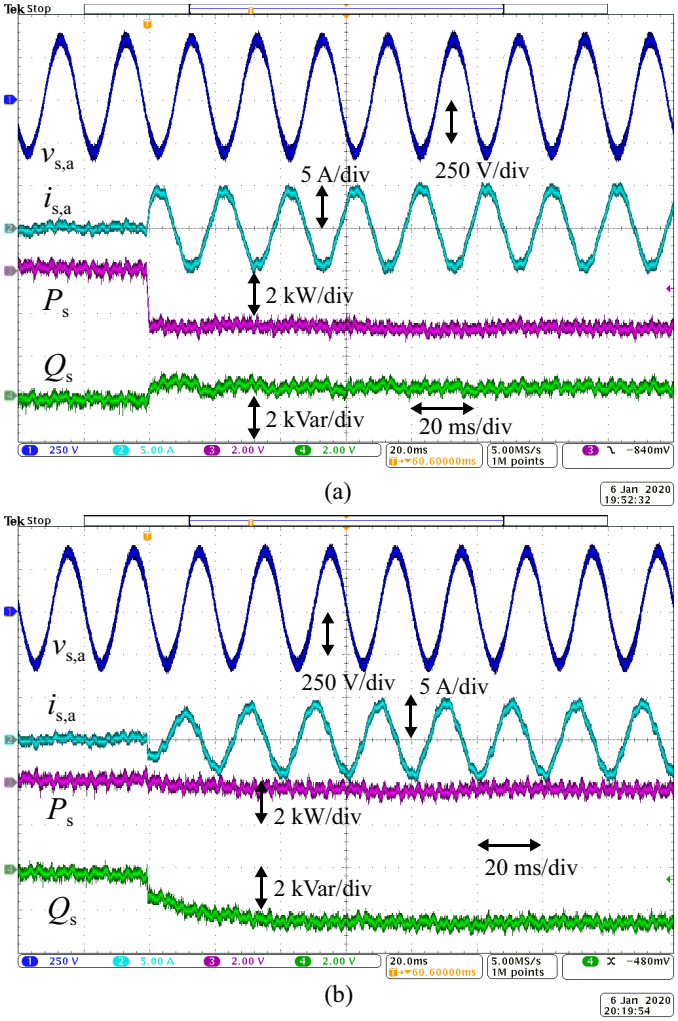


Fig. 16. Measured performance of DFIG system with VOC during active and reactive reference power steps. (a) Active power reference change from 0 kW to 2.3 kW. (b) Reactive power reference change from 0 kVar to 2.0 kVar. Blue: $v_{s,a}$ [250 V/div]; sky blue: $i_{s,a}$ [5 A/div], bubble pink $P_s$ [2 kW/div], and green: $Q_s$ [2 kVar/div].

voltage of the experimental platform is produced by the grid, which is not ideal. The THD of the grid voltage is 1.66%, which mainly contains 1% 5th, 0.8% 7th harmonics due to the background distortion. The harmonics of grid voltage affects the control performance and it influences the output stator current since no harmonic suppression is considered in the controllers. The parameters of the experimental prototype are shown in Table III. A prototype controlled by the traditional VOC method as discussed in [39] is tested for comparison. The active power control loop has an open-loop structure, which is directly controlled by the current on the $d-$ axis. The reactive power control loop is a traditional PI feed-forward control, having an outer-power loop, and an inner-current loop structure.

### A. Comparison of Steady-State and Transient Performance

Fig. 16 shows the transient response and steady-state performance of the DFIG system using the VOC. Two reference steps $\Delta P_s^* = 0.23$ kW and $\Delta Q_s^* = 2$ kVar are set separately to test the transient dynamics of the controllers. Since the active power control is an open-loop structure, the speed of active power response is faster than the reactive power response. The reactive power control loop of the tested VOC is a conventional method, where the time response of reactive power is about 60 ms. Fig. 17 describes the transient performance of the system using the proposed VM-DPC at power reference steps. It is observed that the convergence time is less than 5 ms, and there is nearly no overshoot of the active and reactive power response, which is in accordance with the simulation result. Consequently, it can be concluded that the PI feed-forward structure successfully compensates the coupling between the two loops.

The stator current performance and THD analysis while using the VOC and the proposed VM-DPC are shown in Fig. 18 and Fig. 19, respectively. It is observed that the THD of the stator current when using the VOC is 6.03%. The current THD when using the proposed improved VM-DPC is 4.87%, which is less than VOC. Therefore, it is concluded that the proposed strategy works well in an actual grid condition.

### B. Robustness to Parameter Mismatch

The robustness of DFIG using the proposed VM-DPC is also tested in the experimental prototype as shown in Fig. 20. It can be seen that the system maintains a fast power transient response and satisfied steady-state performance with $+30\%L_m$ and $+30\%R_r$ parameter error. The differences between Fig. 20 and Fig. 17 are barely noticeable.

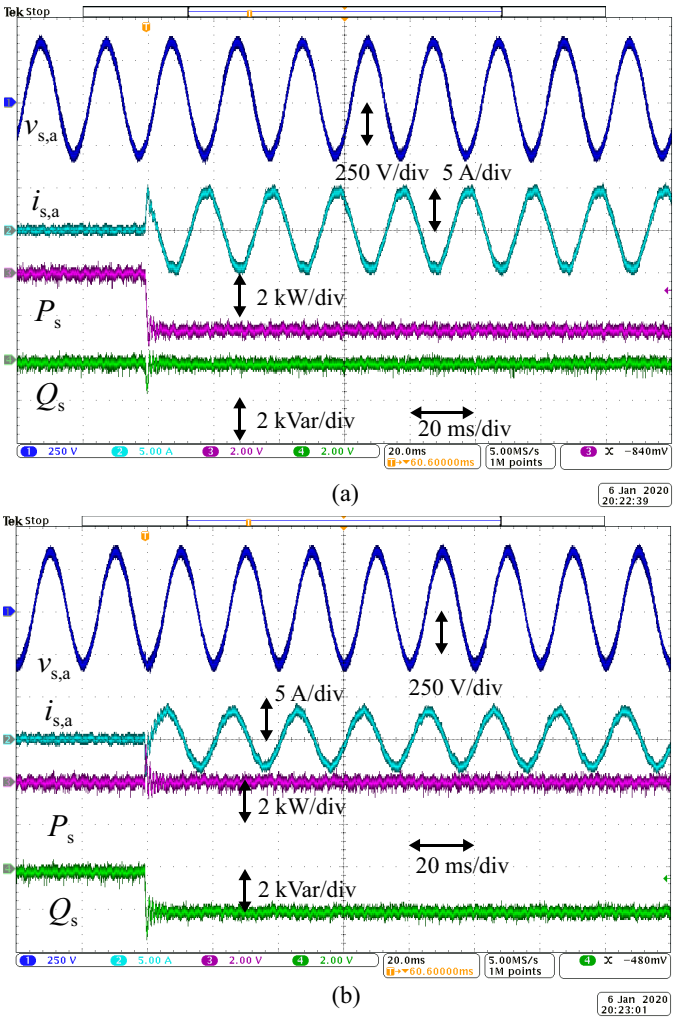


Fig. 17. Measured performance of DFIG system with proposed improved VM-DPC during active and reactive reference power steps. (a) Active power reference change from 0 kW to 2.3 kW. (b) Reactive power reference change from 0 kVar to 2.0 kVar. Blue: $v_{s,a}$ [250 V/div]; sky blue: $i_{s,a}$ [5 A/div], bubble pink $P_s$ [2 kW/div], and green: $Q_s$ [2 kVar/div].

## VII. Conclusion

In this paper, a robust yet straightforward improved VM-DPC control algorithm for the BTB converter of the DFIG system was presented. The proposed method is consisting of a simple feed-forward and feed-back structure without PLL and Park transformation, which reduces the computational burden and simplifies the structure. The proposed method guarantees global exponential stability. Moreover, the stability of the proposed VM-DPC under weak-grid condition is also verified by using eigenvalue analysis and simulations. The proposed VM-DPC is compared with three different control strategies. The results show the proposed VM-DPC can achieve satisfactory steady-state performance with a stator current THD = 1.42%, which is the same level as the conventional VOC. Furthermore, the proposed method also provides a fast transient response with a power convergence time about 1 ms. The robustness of the proposed VM-DPC against parameter variations and slight grid faults is also verified. Finally, the experimental results indicate that the proposed VM-DPC is capable of operating

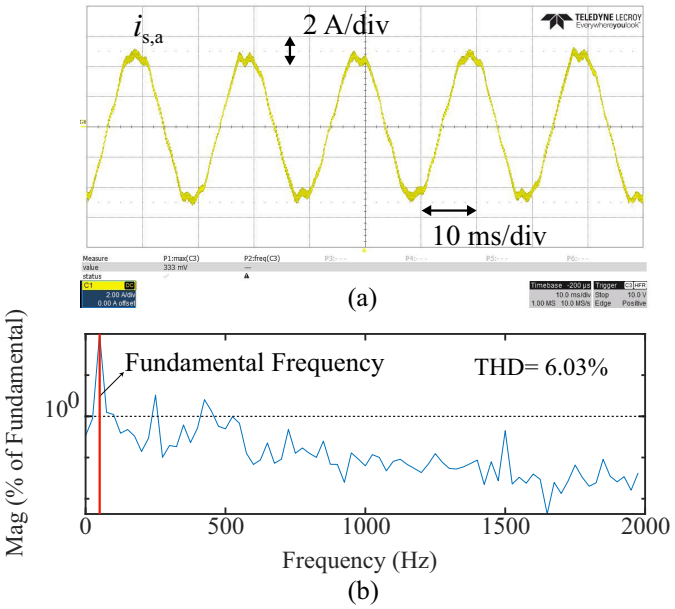


Fig. 18. Stator current spectrum of system using VOC at steady-state $P_s = 2.3$ kW, $Q_s = 0$ kVar. (a) Stator current waveform. (b) Stator current harmonic spectrum.

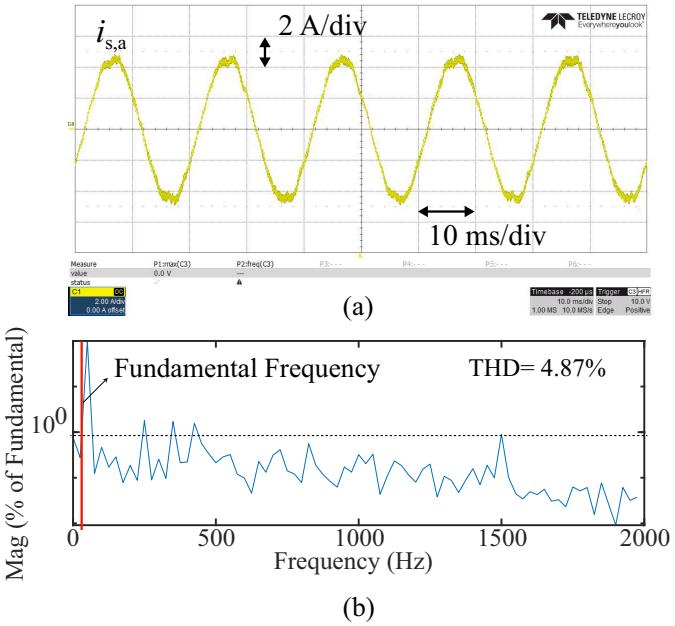


Fig. 19. Stator current spectrum of system using the proposed improved VM-DPC in steady-state $P_s = 2.3$ kW, $Q_s = 0$ kVar. (a) Stator current waveform. (b) Stator current harmonic spectrum.

in an actual grid condition, in which the THD of the stator current is 4.87%.

Our future perspective about the proposed control algorithm includes an investigation on its frequency impedance characteristics, advanced LVRT strategy, and a further improvement under unbalanced voltage conditions.

## Appendix

The authors would like to thank the National Key R&D Program of China (2018YFB0904004) for the financial support.

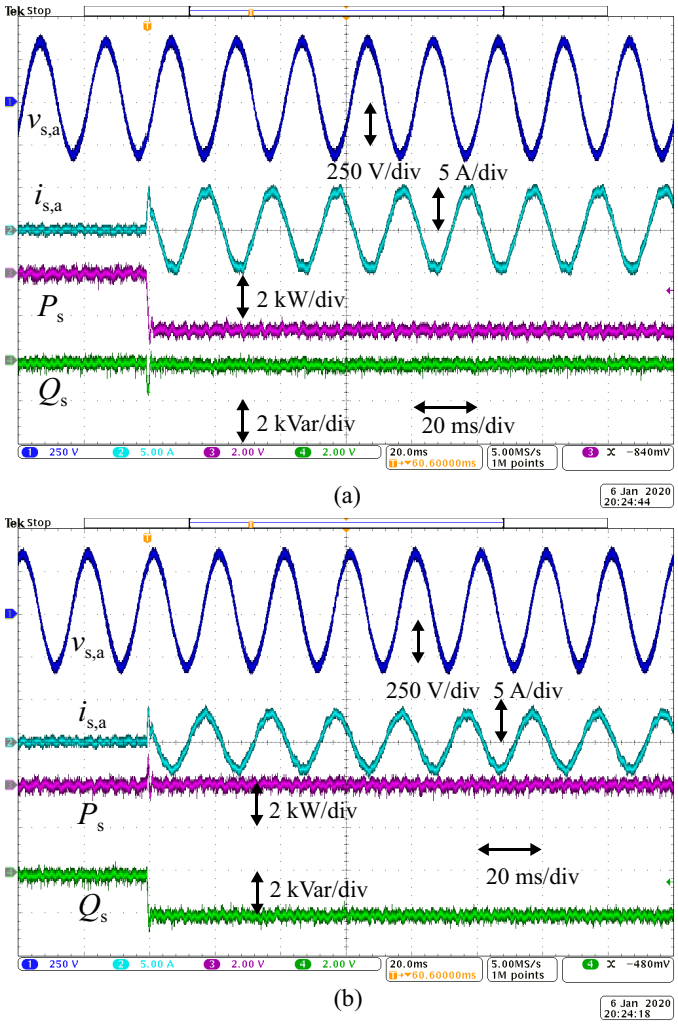


Fig. 20. Measured performance of DFIG system using proposed VM-DPC with $+30\%L_{\mathrm{m}}$ and $+30\%R_{\mathrm{r}}$ parameters mismatch during active and reactive reference power steps. (a) Active power reference change from 0 kW to 2.3 kW. (b) Reactive power reference change from 0 kVar to 2.0 kVar. Blue: $v_{\mathrm{s,a}}$ [250 V/div]; sky blue: $i_{\mathrm{s,a}}$ [5 A/div], bubble pink $P_{\mathrm{s}}$ [2 kW/div], and green: $Q_{\mathrm{s}}$ [2 kVar/div].

## REFERENCES


[1] M. Liserre, R. Cárdenas, M. Molinas, and J. Rodriguez, "Overview of multi-MW wind turbines and wind parks," *IEEE Trans. Ind. Electron.*, vol. 58, pp. 1081–1095, April 2011.

[2] Q. Wu and Y. Sun, *Modeling and Modern Control of Wind Power*. John Wiley & Sons, 2018.

[3] K. Strunz, E. Abbasi, and D. N. Huu, "DC microgrid for wind and solar power integration," *IEEE J. Emerg. Sel. Top. Power Electron.*, vol. 2, no. 1, pp. 115–126, 2014.

[4] D. Koraki and K. Strunz, "Wind and solar power integration in electricity markets and distribution networks through service-centric virtual power plants," *IEEE Trans. Power Syst.*, vol. 33, no. 1, pp. 473–485, 2018.

[5] F. Blaabjerg, Y. Yang, D. Yang, and X. Wang, "Distributed power-generation systems and protection," *Proc. IEEE*, vol. 105, no. 7, pp. 1311–1331, 2017.

[6] D. Zhou, G. Zhang, and F. Blaabjerg, "Optimal selection of power converter in DFIG wind turbine with enhanced system-level reliability," *IEEE Trans. Ind. Appl.*, vol. 54, no. 4, pp. 3637–3644, 2018.

[7] J. Hu, Y. He, L. Xu, and B. W. Williams, "Improved control of DFIG systems during network unbalance using PI-R current regulators," *IEEE Trans. Ind. Electron.*, vol. 56, no. 2, pp. 439–451, 2009.

[8] C. Liu, F. Blaabjerg, W. Chen, and D. Xu, "Stator current harmonic control with resonant controller for doubly fed induction generator," *IEEE Trans. Power Electron.*, vol. 27, no. 7, pp. 3207–3220, 2012.

[9] D. Zhu, X. Zou, L. Deng, Q. Huang, S. Zhou, and Y. Kang, "Inductance-emulating control for DFIG-based wind turbine to ride-through grid faults," *IEEE Trans. Power Electron.*, vol. 32, no. 11, pp. 8514–8525, 2017.

[10] Z. Miao, "Impedance-model-based SSR analysis for type 3 wind generator and series-compensated network," *IEEE Trans. Energy Convers.*, vol. 27, no. 4, pp. 984–991, 2012.

[11] G. Abad, M. A. Rodriguez, and J. Poza, "Two-level VSC based predictive direct torque control of the doubly fed induction machine with reduced torque and flux ripples at low constant switching frequency," *IEEE Trans. Power Electron.*, vol. 23, no. 3, pp. 1050–1061, 2008.

[12] P. Zhou, Y. He, and D. Sun, "Improved direct power control of a DFIG-based wind turbine during network unbalance," *IEEE Trans. Power Electron.*, vol. 24, no. 11, pp. 2465–2474, 2009.

[13] X. Lie and P. Cartwright, "Direct active and reactive power control of DFIG for wind energy generation," *IEEE Trans. Energy Convers.*, vol. 21, no. 3, pp. 750–758, 2006.

[14] H. Nian, Y. Song, P. Zhou, and Y. He, "Improved direct power control of a wind turbine driven doubly fed induction generator during transient grid voltage unbalance," *IEEE Trans. Energy Convers*, vol. 26, no. 3, pp. 976–986, 2011.

[15] L. Shang and J. Hu, "Sliding-mode-based direct power control of grid-connected wind-turbine-driven doubly fed induction generators under unbalanced grid voltage conditions," *IEEE Trans. Energy Convers.*, vol. 27, no. 2, pp. 362–373, 2012.

[16] H. Nian and Y. Song, "Direct power control of doubly fed induction generator under distorted grid voltage," *IEEE Trans. Power Electron.*, vol. 29, no. 2, pp. 894–905, 2014.

[17] H. Nian, P. Cheng, and Z. Q. Zhu, "Coordinated direct power control of DFIG system without phase locked loop under unbalanced grid voltage conditions," *IEEE Trans. Power Electron.*, vol. 31, no. 4, pp. 2905–2918, 2016.

[18] P. Xiong and D. Sun, "Backstepping-based DPC strategy of a wind turbine-driven DFIG under normal and harmonic grid voltage," *IEEE Trans. Power Electron.*, vol. 31, no. 6, pp. 4216–4225, 2016.

[19] S. Boubzizi, H. Abid, A. El, and M. Chaabane, "Comparative study of three types of controllers for DFIG in wind energy conversion system," *Prot. Control Mod. Power Syst.*, vol. 3, no. 3, pp. 214–225, 2018.

[20] S. Mensou, A. Essadki, T. Nasser, and B. B. Idrissi, "A direct power control of a DFIG based-WECS during symmetrical voltage dips," *Prot. Control Mod. Power Syst.*, vol. 5, no. 1, p. 5, 2020.

[21] S. El Daoudi, L. Lazrak, and M. Ait Lafkih, "Sliding mode approach applied to sensorless direct torque control of cage asynchronous motor via multi-level inverter," *Prot. Control Mod. Power Syst.*, vol. 5, no. 1, 2020.

[22] J. Hu, H. Nian, B. Hu, Y. He, and Z. Q. Zhu, "Direct active and reactive power regulation of DFIG using sliding-mode control approach," *IEEE Trans. Energy Convers.*, vol. 25, no. 4, pp. 1028–1039, 2010.

[23] D. Sun and X. Wang, "Low-complexity model predictive direct power control for DFIG under both balanced and unbalanced grid conditions," *IEEE Trans. Ind. Electron.*, vol. 63, no. 8, pp. 5186–5196, 2016.

[24] X. Wang and D. Sun, "Three-vector-based low-complexity model predictive direct power control strategy for doubly fed induction generators," *IEEE Trans. Power Electron.*, vol. 32, no. 1, pp. 773–782, 2017.

[25] J. Hu, L. Shang, Y. He, and Z. Q. Zhu, "Direct active and reactive power regulation of grid-connected DC/AC converters using sliding mode control approach," *IEEE Trans. Power Electron.*, vol. 26, no. 1, pp. 210–222, 2011.

[26] L. Xiong, J. Wang, X. Mi, and M. W. Khan, "Fractional order sliding mode based direct power control of grid-connected DFIG," *IEEE Trans. Power Syst.*, vol. 33, no. 3, pp. 3087–3096, 2018.

[27] Y. Gui, C. Kim, C. C. Chung, J. M. Guerrero, Y. Guan, and J. C. Vasquez, "Improved direct power control for grid-connected voltage source converters," *IEEE Trans. Ind. Electron.*, vol. 65, no. 10, pp. 8041–8051, 2018.

[28] Y. Gui, F. Blaabjerg, X. Wang, J. Bendtsen, D. Yang, and J. Stoustrup, "Improved dc-link voltage regulation strategy for grid-connected converters," *IEEE Trans. Ind. Electron.*, 2020, to be published, doi: 10.1109/TIE.2020.2989720.

[29] Y. Gui, X. Wang, F. Blaabjerg, and D. Pan, "Control of grid-connected voltage-source converters: the relationship between direct-power control and vector-current control," *IEEE Ind. Electron. Mag.*, vol. 13, pp. 31–40, June 2019.

[30] Y. Gui, X. Wang, H. Wu, and F. Blaabjerg, "Voltage-modulated direct power control for a weak grid-connected voltage source inverters," *IEEE Trans. Power Electron.*, vol. 34, pp. 11383–11395, Nov 2019.

[31] Y. Gui, B. Wei, M. Li, J. M. Guerrero, and J. C. Vasquez, "Passivity-based coordinated control for islanded AC microgrid," *Appl. Energy*, vol. 229, pp. 551–561, 2018.

[32] R. Wai and Y. Yang, "Design of backstepping direct power control for three-phase PWM rectifier," *IEEE Trans. Ind. Appl.*, vol. 55, no. 3, pp. 3160–3173, 2019.

[33] W. Gil-González, O. D. Montoya, and A. Garces, "Direct power control for VSC-HVDC systems: An application of the global tracking passivity-based PI approach," *Int. J. Electr. Power Energy Syst.*, vol. 110, pp. 588 – 597, 2019.

[34] Y. Gui, M. Li, J. Lu, S. Golestan, J. M. Guerrero, and J. C. Vasquez, "A voltage modulated DPC approach for three-phase PWM rectifier," *IEEE Trans. Ind. Electron.*, vol. 65, pp. 7612–7619, Oct 2018.

[35] G. Abad, J. López, M. Rodríguez, L. Marroyo, and G. Iwanski, *Vector Control Strategies for Grid-Connected DFIM Wind Turbines*, pp. 303–361. 2011.

[36] L. Zhang, L. Harnefors, and H. P. Nee, "Interconnection of two very weak AC systems by VSC-HVDC links using power-synchronization control," *IEEE Trans. Power Syst.*, vol. 26, no. 1, pp. 344–355, 2011.

[37] D. Yang, X. Wang, F. Liu, K. Xin, Y. Liu, and F. Blaabjerg, "Adaptive reactive power control of PV power plants for improved power transfer capability under ultra-weak grid conditions," *IEEE Trans. Smart Grid*, vol. 10, no. 2, pp. 1269–1279, 2019.

[38] G. Abad, J. López, M. Rodríguez, L. Marroyo, and G. Iwanski, *Steady State of the Doubly Fed Induction Machine*, pp. 155–208. 2011.

[39] D. Zhou and F. Blaabjerg, "Bandwidth oriented proportional-integral controller design for back-to-back power converters in DFIG wind turbine system," *IET Renew. Power Gener.*, vol. 11, no. 7, pp. 941–951, 2017.

[40] "IEEE recommended practice and requirements for harmonic control in electric power systems," *IEEE Std 519-2014 (Revision of IEEE Std 519-1992)*, pp. 1–29, 2014.

[41] I. Villanueva, A. Rosales, P. Ponce, and A. Molina, "Grid-voltage-oriented sliding mode control for DFIG under balanced and unbalanced grid faults," *IEEE Trans. Sustain. Energy*, vol. 9, no. 3, pp. 1090–1098, 2018.


**Shuning Gao** (S'17) received the B.S. degree in electrical engineering from Huazhong University of Science and Technology, Wuhan, China, in 2015. He is currently working toward the Ph.D. degree in the Shandong University.

In December 2019, he was a visiting student with the Automation & Control Section, Department of Electronic Systems, Aalborg University. His research interests include modeling and control of power electronics, stability analysis of power electronics based power systems.

**Haoran Zhao** (S'12-M'15-SM'17) received the B.E. degree from Shandong University, China, in 2005, the M.E. degree from the Technical University of Berlin, Germany, in 2009, and the Ph.D. degree from Technical University of Denmark, Denmark, in 2014. Currently, he is a professor with the School of Electrical Engineering, Shandong University, China.

He was an Electrical Engineer with State Grid Corporation of China (SGCC), in 2005. From 2010 to 2011, he worked as an Application Developer in DIgSILENT GmbH, Germany. His research interests include modeling and integration study of wind power, control of energy storage system, and integrated energy systems.

**Yonghao Gui** (S'11-M'17-SM'20) received the B.S. degree in automation from Northeastern University, Shenyang, China, in 2009, and the M.S. and Ph.D. degrees in electrical engineering from Hanyang University, Seoul, South Korea, in 2012 and 2017, respectively.

From Feb. 2017 to Nov. 2018, he worked with the Department of Energy Technology, Aalborg University, Aalborg, Denmark, as a Postdoctoral Researcher. Since Dec. 2018, he has been working with the Automation & Control Section, Department of Electronic Systems, Aalborg University, Aalborg, Denmark, where he is currently an Assistant Professor. His research interests include Control of Power Electronics in Power Systems, Energy Internet, and Smart Grids.

Dr. Gui has served as an Associate Editor for the IEEE ACCESS and the International Journal of Control, Automation and Systems (IJCAS). He was a recipient of the IEEE Power & Energy Society General Meeting Best Conference Paper Award in 2019 the IJCAS Academic Activity Award 2019.

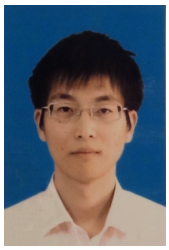

**Dao Zhou** (S'12-M'15-SM'18) received the B.S. from Beijing Jiaotong University, Beijing, China, in 2007, the M. S. from Zhejiang University, Hangzhou, China, in 2010, and the Ph.D. from Aalborg University, Aalborg, Denmark, in 2014, all in electrical engineering.

Since 2014, he has been with Department of Energy Technology, Aalborg University, where currently he is an Assistant Professor. His research interests include modeling, control, and reliability of power electronics in renewable energy application.

**Frede Blaabjerg** (S'86-M'88-SM'97-F'03) was with ABB-Scandia, Randers, Denmark, from 1987 to 1988. From 1988 to 1992, he got the PhD degree in Electrical Engineering at Aalborg University in 1995. He became an Assistant Professor in 1992, an Associate Professor in 1996, and a Full Professor of power electronics and drives in 1998. From 2017 he became a Villum Investigator. He is honoris causa at University Politehnica Timisoara (UPT), Romania and Tallinn Technical University (TTU) in Estonia.

His current research interests include power electronics and its applications such as in wind turbines, PV systems, reliability, harmonics and adjustable speed drives. He has published more than 600 journal papers in the fields of power electronics and its applications. He is the co-author of four monographs and editor of ten books in power electronics and its applications.

He has received 32 IEEE Prize Paper Awards, the IEEE PELS Distinguished Service Award in 2009, the EPE-PEMC Council Award in 2010, the IEEE William E. Newell Power Electronics Award 2014, the Villum Kann Rasmussen Research Award 2014, the Global Energy Prize in 2019 and the 2020 IEEE Edison Medal. He was the Editor-in-Chief of the IEEE TRANSACTIONS ON POWER ELECTRONICS from 2006 to 2012. He has been Distinguished Lecturer for the IEEE Power Electronics Society from 2005 to 2007 and for the IEEE Industry Applications Society from 2010 to 2011 as well as 2017 to 2018. In 2019-2020 he serves a President of IEEE Power Electronics Society. He is Vice-President of the Danish Academy of Technical Sciences too. He is nominated in 2014-2019 by Thomson Reuters to be between the most 250 cited researchers in Engineering in the world.